Suboxic conditions prevailed during the Toarcian Oceanic Anoxic Event in the Alpine-Mediterranean Tethys: the Sogno Core pelagic record (Lombardy Basin, northern Italy)

Gambacorta, G. [1], Cavalheiro, L. [1], Brumsack, H.-J. [2], Dickson, A.J. [3], Jenkyns, H.C. [4], Schnetger, B. [2], Wagner, T. [5], Erba E. [1]

[1] *Dipartimento di Scienze della Terra, Università degli Studi di Milano, Milan, Italy*

[2] *Institute for Chemistry and Biology of the Marine Environment (ICBM), University of Oldenburg, Oldenburg, Germany*

[3] *Centre of Climate, Ocean and Atmosphere, Department of Earth Sciences, Royal Holloway University of London, Egham, Surrey, TW20 0EX, U.K.*

[4] *Department of Earth Sciences, University of Oxford, South Parks Road, Oxford, OX1 3AN, U.K.*

[5] *The Lyell Centre, Global Research Institute, Heriot-Watt University, Edinburgh, EH14 4AS, U.K.*

Corresponding author email: gabriele.gambacorta@guest.unimi.it, phone: +39 02503 15530

Keywords: Jurassic, OAEs, black shale, trace metals, biomarkers, Fish Level

ABSTRACT

The Sogno Core represent one of the deepest pelagic records of the Toarcian Oceanic Anoxic Event (T-OAE) in the Alpine-Mediterranean Tethys. New sedimentological, elemental, Rock-Eval, and biomarker data are presented here, with the aim of reconstructing the depositional conditions that characterized the sedimentation of this succession during the broad positive carbon-isotope excursion of the T-OAE, and its negative isotopic anomaly (Jenkyns Event). Higher Mn_{xs} concentrations, inversely correlated with the $\delta^{18}O$ curve, were observed starting slightly below the onset level of the Jenkyns Event up to the lowermost part of the negative carbon-isotope anomaly, reflecting a combination of a gradual warming and a progressive increase in fresh waters delivered by runoff. Increased weathering intensity was accompanied by enhanced detrital input with higher concentrations in lithogenic elements, and by a relative increase in palaeoproductivity, consistently with higher Si_{xs} concentrations and changes in calcareous nannoplankton assemblages. The enhanced fresh-water input favored water-column stratification, less efficient deep-water circulation and oxygen depletion. Except for two discrete black shales characterized by anoxic pore waters, redox conditions at Sogno turned at maximum suboxic, as indicated by rare to absent bioturbation, limited enrichments in redox-sensitive elements, and molecular biomarkers. The Sogno Core record shows that dominant oxic–suboxic conditions were present also at bathyal depths in the Alpine-Mediterranean Tethys during the Jenkyns Event, thereby contrasting with the anoxic–euxinic environments present both in the shallower water basins and sub-basins of epicontinental northern Europe and, locally, in the relatively deep-water areas of the Alpine Tethys.

1. INTRODUCTION

The Toarcian Oceanic Anoxic Event (T-OAE) was marked by globally distributed deoxygenated waters associated with the accelerated accumulation of organic matter from pelagic to coastal settings (Jenkyns, 1985, 1988, 2010). The T-OAE, originally identified based on the widespread record of coeval lower Toarcian black shales (Jenkyns, 1985), is characterized by a positive carbon-isotope excursion extending over much of the lower Toarcian (Jenkyns and

Clayton, 1997; Jenkyns, 2003; Xu et al., 2018; Storm et al. 2020). This broad $\delta^{13}C$ positive excursion is interrupted by an abrupt negative carbonate and organic carbon-isotope anomaly in its central portion (Erba et al., 2022) globally observed both in shallow- and deep-marine record as well as in continental archives (Xu et al., 2017; Baroni et al., 2018; Remirez and Algeo, 2020b; Reolid et al., 2021; Silva et al., 2021a and references therein). Thermogenic methane associated with metamorphism of organic-rich sediments (McElwain et al., 2005; Svensen et al., 2007), dissociation of marine or terrestrial clathrates along continental margins and/or terrestrial environments (Hesselbo et al., 2000; Pálfy and Smith, 2000; McElwain et al., 2005; Svensen et al., 2007; Percival et al., 2015; Them et al., 2017; Ruebsam et al., 2019), and volcanogenic CO_2 related to the degassing of the Karoo–Ferrar large igneous province (Percival et al., 2015; Heimdal et al., 2021) have been variously credited with causing the observed negative carbon-isotope anomaly. The extensive broad positive carbon-isotope excursion is attributed to accelerated global marine and lacustrine carbon burial (Jenkyns, 1988, 2010; Fantasia et al., 2018; Xu et al., 2018). Anoxic conditions were accompanied by enhanced continental weathering (Jenkyns, 2003, 2010; Cohen et al., 2004; Ullmann et al., 2013; Percival et al., 2016; Them et al., 2017; Jenkyns and Macfarlane, 2021), increased nutrient input into the oceans (Cohen et al., 2004; Jenkyns, 2010; Percival et al., 2016; Izumi et al., 2018; Kemp et al., 2020), extraordinary warmth (Bailey et al., 2003; Dera et al., 2011; Korte and Hesselbo, 2011; Gómez et al., 2016; Ruebsam et al., 2020b) and major marine transgression (Hallam, 1981; Haq et al., 1987; Hardenbol et al., 1998). These processes would have also enhanced primary productivity (Erba, 2004; Jenkyns, 2010), triggered a biocalcification crisis (Erba, 2004; Mattioli et al., 2004; Tremolada et al., 2005; Casellato and Erba, 2015; Erba et al., 2019a; Reolid et al., 2020) and ocean acidification (Erba, 2004; Trecalli et al., 2012; Casellato and Erba, 2015; Posenato et al., 2018; Müller et al., 2020a; Ettinger et al., 2021).

The most widespread deoxygenated conditions were experienced in north European epicontinental basins and sub-basins (e.g., Schouten et al., 2000; van Breugel et al., 2006; McArthur et al., 2008; Hermoso et al., 2009a, 2013; Trabucho-Alexandre et al., 2012; Lézin et al., 2013; Dickson et al., 2017; Houben et al., 2021) and, albeit to a lesser extent, in the ocean-facing Tethyan continental margin bordering the NW European platform (Figs. 1A and 1B) (e.g., Suan et al., 2016; 2018; Dickson, 2017; Ruebsam et al., 2018; Müller et al., 2020b). Redox data from Tethyan shallow-water locations indicate that anoxic conditions did not develop in the water column in these areas (e.g., Reolid et al., 2012; Rodriguez-Tovar and Reolid, 2013; Fantasia et al., 2019a; Ruebsam et al., 2020a; Silva et al., 2021b), although manganese-calcium and iodine-calcium ratios in peri-Adriatic platform carbonates, in places accompanied by a change to more clay-rich and chert-bearing facies, indicate loss of dissolved oxygen in relatively shallow waters during the T-OAE (Woodfine et al., 2008; Sabatino et al., 2013; Lu et al., 2019). However, the expression of the T-OAE in deeper, fully pelagic Alpine-Mediterranean Tethyan settings has been documented only at some locations, such as sections from Austria (Neumeister et al., 2015; Suan e al., 2016), southern Germany (Ebli et al., 1998), Hungary (Vetö et al., 1997; Suan et al., 2016; Müller et al., 2021), and Italy (Jenkyns et al., 2001; Sabatino et al., 2009; Erba et al., 2022) with TOC maximum values from ~2 up to ~13 %. The Sogno succession, deposited at an estimated palaeowater depth of 1500 m, as tentatively reconstructed in Erba et al. (2022), contains one of the deepest T-OAE records (Figs. 1A and B) and is, therefore, an important archive for characterizing long- and short-term variations in palaeoenvironmental conditions during the T-OAE in deep-water settings close to the relatively open Tethyan–Atlantic realm.

Recently, there has been some debate as to the usage of the terms 'T-OAE' and 'Jenkyns Event' (Reolid et al., 2021). The original definition of the Toarcian OAE, proposed by Jenkyns (1988), later coined as T-OAE by van de Schootbrugge et al. (2005), described a phenomenon based on globally distributed apparently coeval organic-rich black shales dated to the early Toarcian *falciferum* Zone. This definition was then complemented by Jenkyns (2010), where the T-OAE is associated with a broad positive carbon-isotope excursion (CIE) interrupted by an abrupt negative "bite" in its central portion. Müller et al. (2017) who first proposed the use of 'Jenkyns Event', suggested ~~the use of~~ this term as a synonym of T-OAE. Subsequently, Reolid et al. (2020) proposed using T-OAE when dealing with marine deposits with evidence of oxygen-depleted conditions, and the term Jenkyns Event in a wider sense for the global changes that occurred during the early Toarcian, thus including the negative CIE, the occurrence of oxygen-depleted conditions, enhanced organic-carbon accumulation during the negative CIE, climatic changes, and associated biotic crisis in marine and terrestrial ecosystems. The definition by Reolid et al. (2020)~~ it~~ is not unambiguously applicable because the above-mentioned global changes are not synchronous and not always applicable to every basin. Moreover, a precise definition of the beginning and end of the Jenkyns Event was not provided, thus hampering its unambiguous identification and correlation on a regional, supra-regional and global scale. In this work we follow the original definition of T-OAE proposed by Jenkyns (2010), while we identify as Jenkyns Event the characteristic negative isotopic anomaly, as discussed in Erba et al. (2022). Accordingly, stratigraphically we place the onset level of the T-OAE at the beginning of the positive excursion and its end at where the maximum value is recorded (Fig. 1D).

The Jenkyns Event in the Sogno Core is expressed by a carbon-isotope negative excursion of ~3 ‰ in carbonates and ~7 ‰ in organic matter and is associated, in its lowermost part, with the so-called Fish Level (Livello a Pesci), a dark grey to black marl with low $CaCO_3$ content and relatively high TOC content up to ~2.5 % (Tintori, 1977; Gaetani and Poliani, 1978; Erba and Casellato, 2010; Erba et al., 2019b, 2022). Detailed lithostratigraphy, carbon-isotope (both $\delta^{13}C_{carb}$ and $\delta^{13}C_{org}$), $\delta^{18}O$, TOC, and $CaCO_3$ data for the Sogno Core can be found in Erba et al. (2022). In this study we present new sedimentological, elemental, Rock-Eval, and biomarker data for the Sogno Core, with the aim of: (1) identifying variations in the depositional conditions across the T-OAE; (2) estimating variations in redox conditions; (3) reconstructing variations in primary productivity during the T-OAE; and (4) proposing a coherent regional depositional model for the organic-rich layers of the Fish Level.

2. GEOLOGICAL SETTING

The Lombardy Basin (northern Italy) was located in the Alpine-Mediterranean Tethys on a relatively undeformed portion of the continental margin of the Adria microplate (Gaetani, 2010) connected to the proto-Atlantic to the west and the greater Tethys to the east (Figs. 1A and 1B). As a consequence of the initial rifting phase leading to the formation of the Atlantic and Ligurian-Piedmont Oceans, during the latest Triassic–earliest Jurassic, a number of troughs, seamounts and plateaus developed after the fragmentation and drowning of a series of Bahamian-type shallow-water carbonate platforms (Bernoulli and Jenkyns, 1974; Gaetani, 1975, 2010; Winterer and Bosellini, 1981; Jenkyns, 2020). Sedimentation was characteristically differentiated, with the accumulation of thick successions in deeper zones and generally condensed, and commonly stratigraphically incomplete deposits on structural highs (Gaetani, 1975, 2010). Slumps, resedimented bodies, and, locally, megabreccias frequently accumulated along the flanks of these submarine topographic features (Castellarin, 1972; Gaetani and Erba, 1990; Pasquini and Vercesi, 2002; Gaetani, 2010). During the final steps of rifting in the Toarcian–Aalenian interval, the Lombardy Basin continued to deepen, with a pelagic sedimentation strongly controlled by the inherited horst-and-graben topography (Bernoulli and Jenkyns, 1974, 2009; Bosence et al., 2009; Santantonio and Carminati, 2011) (Fig. 1C).

The uppermost Pliensbachian–lower Toarcian section recovered with the Sogno Core was deposited on the pelagic Albenza Plateau within the Lombardy Basin (Gaetani and Erba, 1990; Gaetani, 2010). The Sogno Core (45°47′20.5′′ N, 9°28′30.0′′ E) (Fig. 1D) (Erba et al., 2019b; 2022), was drilled next to the type-section of the Sogno Formation (Gaetani and Poliani, 1978; Jenkyns and Clayton, 1986), along the road SP 179 on the northern slope of Monte Brughetto. The lowermost part of the core recovered about a metre of the grey Domaro Limestone Formation, overlain by about 24 metres of vari-coloured claystones, marlstones and marly limestones, locally cherty, belonging to the Sogno Formation (Fig. 1D). Following Erba et al. (2022), the Jenkyns Event is divided into two isotopic segments: a) a lower one, named J1 where, after a marked decrease, the carbon-isotope curve remains at minimum values, and b) an upper isotopic segment, J2, characterized by a gradual increase back to pre-anomaly values (Fig. 1D). The Fish Level correlates with the base of the isotopic segment J1 and extends only to the very lowermost part of segment J2 (Erba et al., 2022). In the Sogno Core, the Fish Level consists of 5 m of dark grey to black marl, marked by a lower grey interval and an upper black interval (Erba et al., 2022) (Fig. 1D). Within the lower grey interval two lithological units (LU) are distinguished (Erba et al., 2019b): a lower LU 7 characterized by grey, to very dark-grey and dark red marly limestones, and a LU 6 consisting of grey to very dark-grey marly limestones with reddish to greyish spots. The upper black interval, coincident with LU 5 (Erba et al. 2019b), is characterized by well-laminated shale with common pyrite nodules. Two discrete occurrences of black shale were also observed about 60 cm above the Fish Level, within the lowermost part of the isotopic segment J2 (LU 4 *sensu* Erba et al., 2019b), in particular a 1 cm-thick lowermost black shale and a 2 cm-thick upper black shale, here named BS 1 and BS 2, respectively. An earlier study has shown that the Fish Level at Sogno is characterized by low calcium carbonate content, with average values of 23.5 %, and total organic carbon (TOC) content progressively rising from ~ 0.2 % in the lowermost part of LU 7 to ~1.4 %, with peaks up to 2.5 % in the uppermost part of LU 5 (Erba et al., 2022).

3. MATERIAL AND METHODS

3.1. Elemental data (XRF)

A total of 170 samples, collected approximately every 10 cm in stratigraphic depth within the Fish Level and 20 cm in the intervals stratigraphically above and below, were analyzed for elemental concentrations by X-ray fluorescence analysis (XRF) at the University of Oldenburg, 60 of which derived from the Fish Level interval. About 700 mg of sample powder were mixed with 4200 mg lithium tetraborate, pre-oxidized in an oven at 500°C overnight with NH_4NO_3 and then fused to glass beads. The beads were analyzed by a wave-length dispersive X-ray fluorescence (WD-XRF) spectrometer equipped with a rhodium tube (Axios Plus, Panalytical®). XRF measurements are based on a calibration with 56 international reference samples covering a wide range in sediment composition. Precision was checked by two in-house standards Peru-1 (fine-grained sediment taken from the upwelling area of the Peruvian margin) and PS-S (Lower Jurassic Posidonia Shale). Analytical precision is better than 1 % for Si, Ti, Al, Fe, Mg, Mn, Ca, K, P, Sr, 2 % for Ba, Cr, Cu, Mo, Ni, Rb, V, Zn, Zr, and better than 5% for Na and Y, except As, Co, Pb (5–10 %).

Elemental concentrations were normalized to Al in order to account for dilution effects. Concentrations are compared relative to the reference average crustal rocks or average shale (AS) element abundance of Wedepohl (1971, 1991) and expressed as element enrichment ($\mathrm{element}_{\mathrm{EF}}$). Enrichment factors were computed using the following formula:

$$\mathrm{element}_{\mathrm{EF}} = (\mathrm{element/Al})_{\mathrm{samp}}/(\mathrm{element/Al})_{\mathrm{AS}} \qquad (1)$$

where $(\mathrm{element/Al})_{\mathrm{samp}}$ is the ratio between the element and aluminium content in a sample, and $(\mathrm{element/Al})_{\mathrm{AS}}$ is the ratio between the element and aluminum abundance in the average shale. We consider an $\mathrm{element}_{\mathrm{EF}} > 3$ as a detectable enrichment and an $\mathrm{element}_{\mathrm{EF}} > 10$ a moderate to strong authigenic enrichment (e.g., Tribovillard et al., 2006; Algeo and Tribovillard, 2009). Similarly, we interpret an $\mathrm{element}_{\mathrm{EF}} < 0.7$ as a detectable depletion and an $\mathrm{element}_{\mathrm{EF}} < 0.1$ as a moderate to strong authigenic depletion. Element concentrations above “normal” detrital background are expressed as element excess ($\mathrm{element}_{\mathrm{xs}}$) using the following formula:

$$[\mathrm{element}]_{\mathrm{xs}} = [\mathrm{element}]_{\mathrm{samp}} - (\mathrm{element/Al})_{\mathrm{bg}} \times [\mathrm{Al}]_{\mathrm{samp}} \qquad (2)$$

where $(\mathrm{element/Al})_{\mathrm{bg}}$ was selected as the lowest element/Al ratio in the dataset (Brumsack, 2006; Meinhardt et al., 2016). Element/Al background values used to estimate excess concentrations for Zr, Si, and Mn are reported in Table S1 in the Supplementary material.

3.2. Pyrite and bioturbation distribution

A rectangular shaped mask, with a length equal to the diameter of the Sogno Core and a width of 2-cm was used to carry out semi-quantitative visual analysis of pyrite and bioturbation distribution from about a metre above to about a metre below the Fish Level interval. The mask, parallel to the bedding of the analysed sediment, was translated every 2 cm to achieve a (from about 11.3 m to 18.3 m) continuous record (Appendix A, Figure S1). Presence and absence of bioturbation, burrow maximum and minimum dimensions, and percentage abundance of burrows were determined for each 2-cm interval. Abundance of burrows was expressed as a percentage of the entire window following Bacelle and Bosellini (1965). The occurrence of pyrite was determined by distinguishing three different classes: nodular pyrite (ovoid to spherical, locally irregular, with sizes > 1 mm), powdery fine-grained pyrite dispersed within the matrix (with sizes < 0.1 mm), and laminar pyrite (distributed as mm-thick continuous laminae).

3.3. Rock-Eval analysis

Rock-Eval Pyrolysis was performed using a Rock-Eval 6 analyzer (Behar et al., 2001) at the Department of Earth Sciences at Oxford University on 79 samples, 60 of which derive from the Fish Level. Samples were collected approximately every 5 to 10 cm in stratigraphic depth. The in-house standard SAB134 (Blue Lias organic-rich marl) was regularly measured (every 8 to 10 samples). The standard deviation on TOC and HI of the in-house standard (SAB134) was 0.11 % and ±29.95 mgHC/g TOC, respectively.

3.4. Lipid biomarker measurements

Aliquots (~6 grams) from a sub-set of 14 samples (freeze-dried and ground), with a sampling rate of approximately 50 cm in stratigraphic depth, were extracted with an Accelerated

Solvent Extractor (DIONEX ASE 350 System), using a mixture of dichloromethane (DCM)/methanol (MeOH) (5:1, v/v) at a temperature of 100 °C and a pressure of 69±10 psi. Sulfur-free extracts (desulfurization by acid-activated copper turnings) were purified by column chromatography over self-packed silica gel (deactivated with 1 % ultrapure H_2O) columns using hexane, hexane:DCM (2:1, v/v), and MeOH as subsequent eluents. The hexane fraction (dissolved in 50µL hexane) was analysed at the Lyell Centre (Heriot-Watt University) on a Thermo Scientific Trace 1310 gas chromatograph (GC) fitted with a split splitless injector (at 280 °C) and linked to a Single Quadrupole Mass Spectrometer using electron ionization (electron voltage 70eV, source temperature 230 °C, quadrupole temperature 150 °C, multiplier voltage 1800V, interface temperature 310 °C). Samples were investigated both in selected ion monitoring (SIM) and in full-scan acquisition mode (50–600 amu/sec), using a thermo fused silica capillary column (60 m × 0.25 mm i.d) coated with 0.25 µm 5 % phenylmethylpolysiloxane phase. The GC temperature was gradually (5 °C/min) increased from 50 to 310 °C, holding the final temperature for 10 minutes and using helium as carrier gas (flow rate of 1 ml/min, initial inlet pressure of 50 kPa, split at 30 ml/min). Reproducibility was monitored using an in-house standard with all targeted compounds and was better than 10 % for all reported biomarker ratios.

4. RESULTS

4.1. Elemental data (XRF)

Average major- and trace-element concentrations, element/Al, standard deviation (1 σ) and maximum values of all the analysed samples and separated for different stratigraphic intervals are reported in Table S2 and Tables S3a –S3 in the Supplementary material, respectively. Enrichment factors based on average shale (AS) (Wedepohl, 1971, 1991) or, when used, local background values

(Appendix A, Table S1), separated for the various intervals, are plotted in Figure 2. Samples stratigraphically below the Fish Level (Appendix A, Table S3a) are enriched in Ca (EF = 115.3), Mn (EF = 13.5), Sr (EF = 7.3), and slightly enriched in Mg (EF = 3.3) and P (EF = 4.0). Samples from LU 7 in the lowermost part of the Fish Level (Appendix A, Table S3b) are enriched in Ca (EF = 9.4) and Mn (EF = 8.0), while they are depleted in Na (EF = 0.4), As (EF = 0.6), Ba (EF = 0.5), U (EF = 0.7), and Zn (EF = 0.7). Samples from LU 6 within the Fish Level (Appendix A, Table S3c) show a similar composition, being enriched in Ca (EF = 8.8), Co (EF = 7.9), Mn (EF = 49.7), slightly enriched in P (EF = 3.2), and depleted in Na (EF = 0.4), Ba (EF = 0.5), U (EF = 0.5), and Zn (EF = 0.7). The upper unit of the Fish Level (LU 5) (Appendix A, Table S3d) is enriched in Ca (EF = 12.2), As (EF = 3.8), Co (EF = 3.1), Mn (EF = 28.8), and Mo (EF = 4.8), and is depleted in Na (EF = 0.5) and U (EF = 0.6). The interval above the Fish Level (Appendix A, Table S3e), without considering the two discrete black shales BS 1 and BS 2, is characterized by enrichments in Ca (EF = 41.5), Mn (EF = 10.9), Sr (EF = 3.8), and depletion in Na (EF = 0.6), Ba (EF = 0.6), Mo (EF = 0.5), Ni (EF = 0.5), U (EF = 0.4). In comparison to AS, black shales BS 1 and BS 2 (Appendix A, Table S3f) are on average enriched in Ca (EF = 34.6), As (EF = 19.1), Co (EF = 10.4), Mn (EF = 22.6), Mo (EF = 10.6), Ni (EF = 4.2), Pb (EF = 5.9), P (EF = 3.5), and Sr (EF = 4.7).

4.2. Pyrite and bioturbation distribution

Variations in bioturbation intensity per unit area and pyrite presence are reported for the interval across the Fish Level (from about 18.3 m to 11.3 m) in Figure 3. Principal ichnotaxa observed in the studied interval are represented by small varieties of *Planolites* and abundant *Chondrites*, testifying to deposition at bathyal water depths (Seilacher, 1967) under oxygen-poor conditions (Bromley and Ekdale, 1984). Bioturbation is very high below the Fish Level in the reddish limestone of LU 8, in the range of 50–100 % per unit area, and sharply decreases in the lowermost part of the Fish level (at about 16.5 m) reaching average values of about 20 % up to the top of LU 7. Discontinuous well-laminated black shales of LU 6 and LU 5 are characterized by sporadic or absent bioturbation with average values of about 2 %. Above the Fish Level, the bioturbation amount sharply increases to average values of 50 %.

Pyrite is visually identified exclusively within the upper part of the Fish level (LU 5) and slightly above it. The distribution of nodular, powdery and laminar (maximum thickness 5 mm) pyrite is reported separately in Figure 3. Nodular pyrite is the most common, with nodules with sizes from ~1 mm up to ~50 mm and abundances of 1 to 7 nodules per unit area. Laminar pyrite is generally rare, displaying discontinuous laminae with maximum lengths of 10–11 cm and maximum thicknesses of 0.5 cm. Powdery pyrite is present and very abundant only in the topmost part of the Fish Level and in BS 1.

4.3. Rock-Eval analysis

In the Sogno Core, HI ranges from 0–438 mgHC/gTOC (Fig. 3). Values close to zero are recorded in samples from LU 8 and in the lowermost part of the Fish Level, whereas a clear increasing trend is observed within LU 6 and LU 5. Above the Fish Level, values return close to zero, returning to values > 200 mgHC/gTOC only in the two organic-rich BS 1 and BS 2 intervals in LU 4. The highest HI values are obtained in the upper black interval of the Fish Level (LU 5), with average values of 300 mgHC/gTOC and peaks up to 440 mgHC/gTOC. T_{max} values range between 426 and 439 °C in all samples, suggesting immature to marginal mature thermal overprint (Figure 4). The Rock Eval data support a mixed marine-terrestrial composition of the kerogen, with a gradual change to oxidized (inert) Type IV kerogen. Higher quality kerogen Type II-mixed

II/III is noted for BS1 and BS2 (note, one sample only) and Fish Level Unit 5, with a gradual transition to Kerogen Type III and IV in units 6 and 7, and sediments from above the Fish Level.

4.4. Lipid biomarker measurements

In this study, biomarker analysis focuses on thermal maturity, and palaeo-environmental conditions including organic-carbon sources, redox and water-column stratification assessment. Results of biomarker measurements are reported stratigraphically in Figure 3.

Thermally unstable 17β,21β(H)-hopanes are either absent or occur in trace amounts only. 17α,21β(H) isomers are predominant compared to the more stable 17β,21α(H) hopanes. In either the αβ and βα isomers, the more stable 22S epimers dominate over 22R, and distributions of the C_{31}-C_{35} homohopanes show a stair-to-step regular pattern with a progressively decrease in peak height and areas from C_{31} to C_{35}. The C_{31} αβ 22S/(22S+22R) homohopane isomerization ratio (Farrimond et al., 1998), which is preferable to the C_{31} homologue, as it presents co-elution with gammacerane in the screened samples, ranges between 0.25 and 0.42 (average 0.36) and it shows no systematic trend upcore or when compared to TOC. Overall, a consistent distribution of the regular (C_{27}, C_{28}, C_{29})-steranes is identified in most samples; sterane isomerization, using the C_{29} ααα 20S/(20S+2-R) ratio (Farrimond et al., 1998) gives results in the range of 0.37 to 0.67, on average 0.48.

The OC sources are assessed based on the relative abundances of chain lengths of *n*-alkanes, which range from *n*C_{15} to *n*C_{35}. High molecular weight (HMW) *n*C_{25} to *n*C_{35} *n*-alkanes shows no odd-over-even pre-dominance, i.e., the average carbon preference index CPI_{25-34} from Bray and Evans (1961) is ~1. The average chain-length ratio (ACL from Peters et. al., 2005) is always <25.

Ratios of pristane (Pr) and phytane (Ph) were used to explore the sources of OM and redox conditions. Pristane and phytane were found in all samples analysed, with an overall predominance of pristane over phytane. The pristane/phytane (Pr/Ph) ratios range between ~1 and 1.9, interrupted only in the upper part of the Fish Level (at ~13 to 12.5 metres), where ratios of about 0.7–0.8 are documented. All higher TOC samples within the Fish Level were screened for lycopane, the occurrence of which is limited to anoxic bottom-water settings (Sinnighe Damsté et al., 2003), and isorenieratene derivatives and related compounds indicative of photic-zone euxinia and a very shallow chemocline (Koopmans et al., 1996). However, none of these compounds were detected in any of the measured samples.

5. DISCUSSION

5.1. Sediment geochemistry

Abundances and stratigraphic distribution of lithogenic conservative elements can be used as tracers of sediment erosion, transport, and depositional processes (Calvert and Pedersen, 2007). Variations in quartz and/or biogenic silica, calcium carbonate mainly of biogenic origin, and clays, the three major components of the studied sedimentary rocks, can be visualized on a triangular diagram with axes SiO_2, CaO, and Al_2O_3 (Fig. 5) (Rachold and Brumsack, 2001). Most samples plot on or close to the so-called ‘carbonate dilution line’ connecting the AS point to the pure carbonate end-member, with only a subtle shift towards higher SiO_2 contents. Sample distribution in this triangular diagram indicates a stable and homogenous background sedimentation dominated by marly limestones and marlstones and biogenic silica. Samples from the Fish Level, due to their lower calcium carbonate content (Erba et al., 2022), plot closer to AS values, indicating a lower amount of dilution by carbonates and/or a higher contribution by clays.

Estimates of grain-size changes in the detrital fraction are derived from Zr, Ti, Rb, and K elemental data. Zr and Ti concentrations are proxies for the coarse- to medium-grained detrital fraction (e.g. Cox et al., 1995; Schneider et al., 1997; Ganeshram et al., 1999; Sageman and Lyons, 2005), whereas Rb and K are considered indicative of the finer grained fraction, in particular aluminosilicate minerals, K-feldspars and clay minerals (Heinrichs et al., 1980; Cox et al., 1995; Calvert and Pedersen, 2007). Concentrations of TiO_2, K_2O, Rb, and Zr plotted versus Al_2O_3 are close to AS values (Wedepohl, 1971, 1991) (Fig. 6; Appendix A, Tables S2 and S3a–S3f), thereby indicating no significant enrichment or depletion in comparison to AS. However, in the SiO_2 versus Al_2O_3 cross-plot (Fig. 6) most of the samples fall well above the AS line, indicating an additional contribution apart from the background detrital flux, most likely from biogenic silica. Observed variations in lithogenic elements suggest an essentially homogeneous detrital source area through time in a low-energy distal depositional setting. The generally low detrital input likely implies low to no dilution of the organic-matter fraction, as confirmed by TOC/Al variation that is rather similar to the variation in the TOC itself (Fig. 3).

Even if most of the studied record reflects relatively stable background sedimentation, the stratigraphic variations in lithogenic elements highlight some intervals characterized by a relatively higher detrital input (Fig. 7). Higher Zr_{xs}, Ti/Al, K/Al, Rb/Al values observed in the sediment close to the Pliensbachian/Toarcian boundary from about 25.5 to 23.0 m (Fig. 7) suggest greater amounts of siliciclastic input, consistent with the sedimentological description by Gaetani and Poliani (1978). A similar trend was observed in coeval British Jurassic sections and interpreted as the result of a global sea-level drop close to the Pliensbachian/Toarcian boundary (e.g., Hesselbo, 2008; Thibault et al., 2018). Detrital input also increased prior to the deposition of the Fish Level, as indicated by higher siliciclastic contents from about 17.5 m reaching its maximum in correspondence with the base of the Fish Level (LU 7), followed by a progressive decrease back to lower values above the Fish Level at about 11.4 m. The rise in Cr/Al at about 17.5 m (Fig. 8), comparable to the trend observed in the lithogenic elements, likely testifies to an increase in abundance of heavy minerals (i.e., chromite) related to detrital input rather than redox conditions. A mainly fluvial origin of the siliciclastic input is here inferred based on the absence of grain-size sorting typical of aeolian deposits (cf. Wang et al., 2017), with enrichments in Si/Al, Ti/Al and Zr/Al ratios (Schnetger, 1992; Schnetger et al., 2000). In fact, the occurrence of similar trends observed in Si, Zr_{xs}, Ti, Rb and K testifies to the combined transport of both the coarse- to medium-grained fraction and the fine-grained components. However, a partial influx from an additional aeolian source cannot be excluded. The observed high Zr_{xs} concentrations in BS 1 and BS 2, not associated with enrichments in other detrital elements apart from a minor increase in the Ti/Al ratios, suggest either a coarser grained input or low sedimentation rates with a poorer dilution of the coarser fraction by fine-grained material. Winnowing can also be a potential process leading to higher Zr_{xs} values due to increases in the proportion of heavy minerals linked to hydrodynamical sorting during periods of increased current velocities. However, the lack of sedimentological evidence for reworking by bottom-water currents seems to exclude such an interpretation. An increase in weathering intensity coupled with higher detrital input, over the time interval registered from about 17.5 m up to about 11.4 m, is inferred based on the observed trend in the K/Al ratio (Fig. 7), used as a proxy for mobile versus immobile elements (Clift et al., 2008; Dickson et al., 2010). Furthermore, a change in the clay fraction is deduced from the K/Rb ratio (Fig. 7) showing elevated values in the uppermost part of the record, interpreted as a possible shift to higher illite content (Rothwell et al., 2006) from 17.5 m upwards.

Mn-rich carbonates have been observed in a number of deep-marine Alpine-Mediterranean Tethyan sections of Toarcian age (e.g., Jenkyns et al., 1991; Vetö et al., 1997; Ebli et al., 1998; Bellanca et al., 1999; Hermoso et al., 2009b; Sabatino et al., 2011; Polgári et al., 2012a, b, 2016; Suan et al., 2016); they were interpreted either as the result of microbially mediated accumulation of Mn within or close to the oxygen minimum zone (Jenkyns et al. 1991, Sabatino et al. 2011), or due to the advection of manganese-rich waters from both proximal and distal hydrothermal activity related to the spreading ridges of the Alpine-Mediterranean Tethys (Polgári et al. 1991; Corbin et al., 2000). However, higher Mn values observed from slightly below the Fish Level at ~17.5 m up to the interval encompassing the entire Jenkyns Event, suggest the presence of an additional input of Mn that added to the already relatively high background values. We speculate that, in this interval, higher Mn concentrations were induced by enhanced riverine input (cf. Elderfield, 1976; Aguilar-Islas and Bruland, 2006; Brumsack, 1991) that sourced additional Mn to the already elevated Mn concentrations typical for pelagic settings. Increased fluvial input (Chester and Jickells, 2012), probably coupled with higher fluxes of organic matter, can possibly explain the observed rise in the Cu/Al ratio present slightly below the interval of the Jenkyns Event, similarly to what is observed on the Mn_{xs} trend (Fig. 8). We point out that the general Mn_{xs} trend is inversely correlated with the $\delta^{18}O$ curve, with oxygen-isotope values decreasing while Mn_{xs} rises. We speculate that observed variations in the oxygen-isotope curve might reflect a gradual warming leading to an accelerated hydrological cycle and progressive increase in fresh water supply of Mn at a time of extensional tectonic activity along the continental margin. Indeed, observed Mn variations may also reflect variations in redox conditions that added to the enhanced Mn supply to the basin. In fact, under reducing conditions Mn could have been more efficiently dissolved from Mn-oxyhydroxides MnO_2 and MnOOH and, when not escaping back to the water column, fixed as Mn(II) into authigenic carbonates (Hild and Brumsack, 1998; Calvert and Pedersen, 1993; Brumsack, 2006; Tribovillard et al., 2006). Based on mass-balance considerations (Rachold and Brumsack, 2001), the redistribution of Mn by redox changes during diagenesis cannot explain the high Mn concentrations observed at Sogno. Therefore, an additional, most likely fluvial Mn source is indicated.

5.2. Redox conditions

Many elements accumulate in marine sediments as a result of adsorption or post-depositional precipitation from bottom waters or from pore waters in response to specific redox conditions (Brumsack, 1980; Algeo and Maynard, 2004; Brumsack, 2006; Lyons and Severmann, 2006; Tribovillard et al., 2006; Calvert and Pedersen, 2007; Piper and Calvert, 2009; Little et al., 2015; Algeo and Li, 2020; Algeo and Liu, 2020). In this work we follow the classification of redox facies proposed by Tyson and Pearson (1991), with oxic conditions associated with oxygen levels > 2.0 ml/l, dysoxic conditions characterized by values between 2.0 and 0.2 ml/l, suboxic between 0.2 and 0 ml/l, anoxic when oxygen content is equal to 0 ml/l, and euxinic when the complete lack of oxygen is accompanied by the presence of free H_2S. Concentrations in redox-sensitive elements are reported in Tables 2 and 3a–3f in the Supplementary material. Redox conditions, reconstructed based on the redox-sensitive elements integrated with bioturbation intensity (Bromley, 1990; Potter et al., 2005) and Pr/Ph ratio (Didyk et al., 1978; Peters et al., 2005), vary strongly within the studied record (Figs. 3 and 8), as described below from bottom to top.

The Domaro Limestone Fm. and the lowermost marly limestones of the Sogno Fm. below the Fish Level document a well-oxygenated depositional setting, as evidenced by the extensive presence of bioturbation and absence of enrichment in redox-sensitive elements (Figs. 2, 3 and 8; Appendix A, Table S3a).

The lowermost part of the Fish Level (LU 7) does not show enrichments or depletions in redox-sensitive elements (Figs. 2, 3 and 8; Appendix A, Tables S3b), and has a Pr/Ph ratio of 1.1. The progressive reduction in bioturbation intensity further testifies to a deterioration of the oxygen levels in the surficial sediments. We interpret the basal part of the Fish Level (LU 7) as deposited under dysoxic conditions at least within pore waters, if not at the sea floor.

The mid-grey to dark-grey marly limestones (LU 6) of the Fish Level mark a transitional phase to higher TOC > 1 % (Erba et al., 2022). This unit shows slight relative enrichment only in Co (Figs. 2, 3 and 8; Appendix A, Table S3c) and has an average Pr/Ph ratio of 1.3. The observed enrichments in Co were likely controlled by Mn-shuttling as oxides and hydroxides rather than being related to anoxic conditions (Calvert and Pedersen, 1996; Tribovillard et al., 2006). However, the absence or extreme rarity of bioturbation testifies to a shift to more dysoxic conditions at the seafloor.

The well-laminated black shales of the upper part of the Fish Level (LU 5), with TOC content up to 2.5 % and highest HI values up to 440 mgHC/gTOC, are characterized by minimal/absent bioturbation and common pyrite (Fig. 3) associated with moderate enrichments of As, Co, and Mo (Figs. 2, 3 and 8; Appendix A, Table S3d). The higher Mn concentrations might have played an important role in controlling the observed concentrations in redox-sensitive elements. Observed enrichments in As and Co were likely induced due to their initial scavenging by Mn-oxides and hydroxides and subsequent early diagenetic incorporation into iron sulfides rather than ambient anoxic conditions (Calvert and Pedersen, 1996; Tribovillard et al., 2006). Also, the observed moderate Mo enrichments are not necessarily related to anoxic/euxinic conditions.

In fact, manganese oxides are usually very effective in removing Mo from seawater into sediments. During the partial loss of Mn to the water column via porewater flux under suboxic conditions, the liberated Mo is released and probably re-fixed as thiolated Mo species and/or in association with organic matter (Neubert et al., 2008; Dahl et al., 2017). We do not observe significant enrichments of other elements associated with reducing conditions, such as Fe, Cu, Ni, Zn, U, V, etc. Based on redox-sensitive elemental associations (Crusius et al., 1996; Algeo and Maynard, 2004; Brumsack, 2006; Lyons and Severmann, 2006; Tribovillard et al., 2006) we interpret this interval as deposited under prevailing suboxic conditions in pore waters. Relatively higher values in redox-sensitive elements in correspondence with or stratigraphically close to the interval with the lowermost values of the negative carbon-isotope anomaly suggests that the most extreme suboxic conditions were probably recorded by this part of the sequence. Even if oxygen availablity was limited, as suggested by lower Pr/Ph ratios down to values < 0.1 in the topmost part of the Fish Level, truly anoxic conditions were never reached over longer time periods. This contention is further confirmed by the absence of lycopane and isorenieratene derivatives and related compounds, thus suggesting that neither bottom- nor shallow-water anoxia occurred. However, short-lived pulses of more extreme redox conditions, not resolvable by the used proxies utilized and by sampling resolution, cannot be excluded.

Above the Fish Level (LU 4), an abrupt increase in bioturbation (about 50 %) suggests a recovery in oxygenation levels concurrent with a decrease in TOC (<1 %), further supported by low concentrations in redox-sensitive elements (Figs. 2, 3 and 8; Appendix A, Table S3e) and a Pr/Ph ratio of about 1.6.

Based on the observed enrichments in As, Co, Mo and Ni and on the slight enrichments in Fe and Zn (Figs. 2, 3 and 8; Appendix A, Table S3f) we infer that the deposition of the two discrete black shales BS 1 and BS 2 above the Fish Level occurred under the influence of anoxic pore waters. The absence of lycopene and isorenieratene derivatives and related compounds suggests that, at least over longer time intervals, anoxia was limited to pore waters without reaching either bottom waters or the photic zone. However, as indicated by the lack of bioturbation, short-lived episodes of anoxia extending also to bottom waters cannot be excluded. Ni and Co, both characterized by a weak euxinic affinity (Algeo and Maynard, 2004), under anoxic conditions tend to be fixed into the insoluble sulfides (NiS and CoS) that can be taken up in solid solution with authigenic pyrite (Huerta-Diaz and Morse, 1990, 1992; Morse and Luther, 1999; Tribovillard et al., 2006). The higher Pr/Ph ratio of about 1.9 measured for BS 1, indicative of relatively oxidizing conditions (Didyk et al., 1978; Peters et al., 2005), contradicts elemental data. However, as described in Large and Gize (1996) and in agreement with the higher Zr concentrations, observed Pr/Ph values can be related to enhanced, early diagenetic, anaerobic oxidation of the organic matter associated with very low sedimentation rates.

The presence of diffused bioturbation and the lack of enrichment in redox-sensitive elements in the uppermost marly limestones (LU 3 to LU 1) (Figs. 2, 3 and 8; Appendix A, Table S3e) indicate that their deposition occurred under fully oxic conditions.

Sweere et al. (2016) proposed using the product of Mn_{EF} and Co_{EF} to discriminate between environments, with values exceeding 2 indicating sedimentation in a restricted basin, and values lower than 0.5 indicating deposition in an upwelling setting. The $Co_{EF} \times Mn_{EF}$ versus Al cross-plot for samples from the Fish Level, BS 1 and BS 2 is shown in Figure 9. All analysed samples from the Fish Level, BS 1 and BS 2 have values > 2, suggesting that their deposition occurred in a stratified setting. In particular, values increase from the base (lowermost LU 7) to the top (LU 5) of the Fish Level, suggesting that local oxygen depletion gradually increased with less efficient deep-water ventilation, thus favoring the burial of labile organic carbon.

5.3. Organic-matter properties: thermal maturity and organic-carbon sources

T_{max} values ranging from about 426 to 439 °C indicate type II and type III kerogens (HI ~200–440) from immature to marginal mature. Incomplete homohopane and iso-sterane isomerisation with average 22S C_{32} $\alpha\beta$ hopane and 20S C29 $\alpha\alpha\alpha$ sterane values <0.5 and <0.6, respectively, suggest that thermal maturity had limited impact on the biomarker compounds (Peters et al., 2005; Farrimond et al., 1998). Therefore, CPI values of ~1 (Fig. 3) likely arise from a stable organic matter type rather than indicating thermal maturity in all screened samples below, within, and above the Fish Level. However, the Rock Eval data, in combination with ACL and Pr/Ph ratios, tend to suggest minor fluctuations in the organic matter composition or quality, indicated by the lower ACL and Pr/Ph values combined with a clear kerogen type II RockEval signature in the more oxygen-depleted LU5. We speculate that this period has produced and preserved the highest fraction of autochthonous marine organic matter in the succession throughout the T-OAE.

We note that kerogen type III-IV in samples with low TOC (≤0.5 %) and HI (<170 mgHC/gTOC) must be treated with caution (Peters et al., 2005). In fact, these samples come from the lower part of the Fish level (LU 7 and LU 6), and/or below or above the Fish Level (Fig. 3), and represent either a combination of well-oxygenated conditions and aerobic organic matter decay (Peters et al., 2005) coupled with a remote terrestrial organic matter background, or a signal of fully degraded labile marine organic matter. (Fig. 3).

5.4. Productivity

Silica excess is frequently used as a reliable proxy for trophic conditions (e.g., Schmitz et al., 1997; Turgeon and Brumsack, 2006; Hu et al., 2009), representing a rough estimate of opaline silica. Stratigraphic variations in Si_{xs} (Fig. 7) indicate a rise in opaline silica that predated the deposition of the Fish Level from about 17.5 m, reaching the highest values in the upper part of the Fish Level (uppermost part of LU 6 and then in the upper half of LU 5) in the lowermost part of isotopic segment J2. Based on Si_{xs} data, relatively high amounts of biogenic silica were produced also after the end of deposition of the Fish level (middle of LU 4), prior to progressively decline through isotopic segment J2. It should be noted that measured variations in Si_{xs} are consistent with the higher concentrations in radiolaria observed in microfacies from the upper part of the Fish Level sampled at the Colle di Sogno outcrop (Casellato and Erba, 2015), suggesting relatively higher trophic conditions favoring siliceous zooplankton during the deposition of the upper black shale interval.

Although the palaeoecological affinities of most Early Jurassic calcareous nannoplankton are still not fully constrained, taxa sensitive to palaeotemperature and palaeofertility have been recognized (Casellato and Erba, 2015; Fraguas et al., 2021; Peti et al., 2021). Calcareous nannofossils were quantitatively investigated in the Colle di Sogno outcrop and the inferred palaeoceanographic changes during the late Early Toarcian can be compared to the geochemically based environments reconstructed from the Sogno Core. During the latest Pliensbachian-earliest Toarcian rather stable oligotrophic conditions promoted the proliferation of deep-dwellers. A combination of higher fertility and disruption of surface-water stability triggered a rapid shift in nannofossil assemblages. Specifically, the Fish Level is characterized by an increase in abundance of *Lotharingius* and *Biscutum* suggesting mesotrophic conditions further corroborated by the drop in abundance of the presumed oligotrophic *Schizosphaerella,* although its crisis is possibly the result also of ocean acidification (Erba, 2004; Casellato and Erba, 2015; Faucher et al., 2022). However, differently from Si_{xs}, mesotrophic calcareous nannoplankton assemblages exhibit a more constant trend within the Fish Level without rising in abundance up-section. Thus, calcareous nannoplankton changes are consistent with the geochemical palaeoproductivity proxies: the Fish Level deposited under enhanced fertility conditions that returned to the pre-Jenkyns Event regime in the early part of the isotopic segment J2.

5.5. Depositional conditions and processes during the T-OAE in the Sogno Core

Inferred variations in the depositional conditions and processes during the T-OAE interval of the Sogno Core are schematically summarized in Figure 10. Eight phases are identified and labelled here for convenience from A to H. Our data indicate that no environmental changes were associated with the onset of the T-OAE in terms of detrital input, primary productivity or reducing conditions. Most of the interval defining the onset of the positive carbon-isotope excursion of the T-OAE (A in Figs. 10 and 11a), was characterized by fully oxic bottom waters and relatively cool temperatures. Slightly before the onset of the Jenkyns Event (B in Figs. 10 and 11a), and preceding the deposition of the Fish Level, depositional conditions changed abruptly. A rise in temperature, as illustrated by oxygen-isotope ratios in bulk carbonate, was accompanied by enhanced weathering, higher runoff and increased detrital input with higher amounts of Mn, Zr and Si delivered to the basin. The increased availability of nutrients favored a slightly higher productivity, despite oxic conditions being present at the sea floor. The higher amounts of manganese delivered to the basin were fixed both in Mn-carbonates and Mn-oxides and hydroxides. We point out that the beginning of warming predates the onset of the negative isotopic excursion of the Jenkyns

Event. During the deposition of the lowermost part of the Fish Level (C in Figs. 10 and 11a), i.e. the lithostratigraphic expression of the Jenkyns Event, established relatively warmer conditions were accompanied by greater detrital sediment transport to the basin. Higher nutrient loads associated with this detrital flux favored a relative rise in primary productivity. The increased input of fresh water coupled with warmer conditions resulted in the establishment of a pycnocline and a less efficient vertical mixing. The subsequent decrease in oxygen content at the sea floor was accompanied by a drastic reduction in the benthic fauna and the escape of Mn back to the water column when not trapped in authigenic Mn-carbonates. The onset of the deposition of the Fish Level is thus the lithological record of a threshold in the environmental conditions capable of switching the sedimentation style from marly limestones, dark-red in colour, with sporadic greyish spots to marly limestones, with variations in colour from grey, to very dark-grey and dark red (Erba et al., 2019a). During this stratigraphic interval, organic matter was either entirely dominated by oxidized marine organic material, or represented by a mix of degraded marine organic matter and continental organic matter brought to the basin by the relatively higher runoff. With the deposition of LU 6 (D in Figs. 10 and 11a) progressively higher temperatures were accompanied by higher runoff and increased organic matter fluxes to the sea floor. Bottom-water oxygen levels further decreased, hindering sediment reworking by benthic organisms, and favoring Mn recycling and fixation of Co in Mn carbonates. The warmest conditions were reached during the deposition of the uppermost part of the Fish Level (LU5, E in Figs. 10 and 11b), characterized by the accumulation of black shales with higher TOC up to 2.5 %. Increased runoff resulted in the most intense water stratification and less efficient bottom-water renewal, with the establishment of suboxic conditions that peaked in intensity during the latest part of isotopic segment J1. The establishment of oxygen-poor conditions enhanced the preservation of the labile marine organic matter that either constituted the entirety of the preserved organic fraction, or represented an additional contribution to the background terrestrial organic matter. Even if reducing conditions were relatively more intense, the fixation of Mn occurred in greater amounts due to the higher rates of fresh water input. Mn-scavenging favored the accumulation of As, Co, and Mo, together with the formation within the sediments of pyrite favored by the degradation of organic matter and the presence of free H_2S in pore waters. Primary productivity, even if low to moderate, was generally more intense during the deposition of the uppermost part of the Fish Level. The interval right above the Fish Level (F in Fig. 10 and 11b) represents the beginning of the recovery after the most intense deoxygenated conditions. Associated with a progressive cooling, runoff declined together with primary productivity and detrital input. The end of the deposition of the Fish Level black shales indicates a change in the environmental conditions from suboxic to fully oxic bottom waters. We speculate that the relatively high amounts of Mn_{xs} in this interval represent a phase of more efficient Mn accumulation due to the changed redox conditions rather than a signal of higher fresh water input. In fact, with the re-establishment of oxic conditions Mn started to be more efficiently fixed in Mn-oxides and hydroxides. Within this interval, the depositional conditions and processes that controlled the sedimentation of black shales BS 1 and BS 2 are indeed enigmatic. Brief pulses in runoff, as probably indicated by higher Zr_{xs} concentrations and a minor increase in the Ti/Al ratios, could have been behind the origin of short-lived intervals of deep-water anoxia. However, an increase in runoff is indeed counterintuitive in a phase characterized by an overall decreasing trend in temperature, weathering, and runoff. Indeed, sedimentation of the black shales occurred under low primary productivity settings and reduced sedimentation rates, possibly pointing to a degree of condensation resulting in concentrate organic matter. The succession deposited in the last part of the Jenkyns Event (G in Fig. 10 and 11b) represents a transitional phase towards normal conditions (H in Fig. 10 and 11b). The late part of the T-OAE shows environmental conditions comparable to those of the pre-T-OAE interval. No changes in surface or bottom waters mark the end of the T-OAE, with stable conditions extending to the middle Toarcian.

5.6. The T-OAE in the Alpine-Mediterranean Tethys

We correlated the Sogno Core with other records from the Alpine-Mediterranean Tethys, the north European epicontinental seaway, and the marginal proto-Atlantic (Tab. 1) characterized by a high-resolution carbon-isotope chemostratigraphy accompanied by elemental and organic geochemical data (Fig. 12). The lithological expression of the T-OAE varies significantly in the various sections and cores considered here. As highlighted by the correlation in Figure 12, deposition of black shale was clearly diachronous, with large differences in the onset and end of organic-rich sedimentation. In all the considered sections no black shales occur before the Jenkyns Event, while their deposition became widespread in correspondence of the interval close to the lowest point in the trough of the negative carbon-isotope anomaly.

Changes in the detrital input in the various sections were recognized by means of lithogenic elemental data. At Peniche (Portugal), Fantasia et al. (2019a) observed within isotopic segment J1 an increase in the detrital index paralleled by high values in the kaolinite/(illite + chlorite) ratio used as a measure of weathering intensity. At Creux de l’Ours (Switzerland), on the basis of whole-rock and clay mineralogy and elemental data, Fantasia et al. (2018) highlighted an increase in detrital input in correspondence with the isotopic segment J1 and the lower part of the isotopic segment J2. Increases in Si/Al, Zr/Al and Ti/Al, together with higher quartz content were observed at Sancerre (France) in the interval deposited during the Jenkyns Event (Hermoso et al., 2013). In particular, higher values were measured close to the base of the isotopic segment J1 and for most of the isotopic segment J2. Detrital elements were also measured at Rietheim (Switzerland) by Montero-Serrano et al. (2015). The stratigraphic variation in lithogenic elements clearly highlights two intervals with higher clastic input, specifically a lower one at the level of the base of the negative isotopic excursion, and an upper one starting close to the top of the isotopic segment J2 that extends above for about 50 cm. In Yorkshire (UK), Thibault et al. (2018) observed changes in the detrital components based on elemental data (Si/Al, Zr/Al, Zr/Rb, etc.). They highlighted a series of intervals across the Jenkyns Event with higher detrital input, in particular: in the lowermost part of the succession in the interval that precedes the negative isotopic anomaly of the Jenkyns Event up to the lowermost part of the isotopic segment J1; in the interval deposited over the transition from J1 to J2; across the uppermost part of the succession recording the isotopic segment J2 and above. No lithogenic elemental data are available for the German records of Dotternhausen and Shandelah. During the Jenkyns Event, global warming associated with increased $p\text{CO}_2$ induced an increase in temperature of 7−10 °C (Ruebsam et al., 2020b) that in the Tethyan region led to an acceleration of the hydrological cycle favoring the increase in continental weathering and runoff (Cohen et al., 2004; Hermoso and Pellenard, 2014; Brazier et al., 2015; Montero-Serrano et al., 2015; Percival et al., 2015; Fantasia et al., 2018). Warm and humid conditions during the Jenkyns Event were reconstructed also by means of palynological data, such as for example from sections in Poland by Pieńkowski et al. (2016). Arid conditions were instead observed at the Peniche section (Rodrigues et al., 2016; Font et al., 2022). However, this difference seems to be related to more local effects, as the Lusitanian Basin during the Toarcian was located at the boundary between warm temperate and arid climatic belts (Font et al., 2022). Dera and Donnadieu (2012) modelled the climatic conditions during the early Toarcian and estimated by means of a coupled ocean–atmosphere model (Fast Ocean Atmosphere Model – FOAM) a 9 cm/yr increase in global precipitation rates and a 3.5 cm/yr increase in mean annual continental runoff. Indeed, a contribution to the observed stratigraphic changes in the detrital proxies could derive from the transgressive–regressive cycles that characterized the early Toarcian, in particular a forced regression before the Jenkyns Event and the broad eustatic transgression that followed immediately thereafter (e.g, Thibault et al., 2018). Additional clastic contributions related to storm activity have been suggested by other authors (Trabucho-Alexandre et al., 2012; Suan et al., 2013; Krencker et al. 2015; Fantasia et al., 2019a). Indeed, common trends in the sections presented in Figure 12 can be recognized, with higher detrital input occurring in the early part of the Jenkyns Event, and a general increase in sections from the shallow-water north European epicontinental seaway. Observed variations, thus, probably reflect a combination of causes controlled by climatic, eustatic and bottom-water physical processes (Remirez and Algeo, 2020a).

An increase in primary productivity is generally observed for sections deposited in the north European epicontinental seaway (Cohen et al., 2004; Montero-Serrano et al., 2015; Percival et al., 2016; Xu et al., 2018; Fantasia et al., 2019a). Higher organic matter fluxes were ascribed to higher levels of nutrient availability delivered from continents by increased runoff. In the Peniche section, Lusitanian Basin, Fantasia et al. (2019a) observed higher values in total P coupled with a slight increase in HI values, which they interpreted as evidence of higher nutrient availability and relatively higher levels of primary productivity. Higher values were observed in correspondence with the early phase of the Jenkyns Event and across the end of isotopic segment J1. At Creux de l'Ours (Switzerland) Ni/Al, Cu/Al and P_{tot} data were used by Fantasia et al. (2018) to infer relatively higher level of productivity in the J1 and lower part of the J2 isotopic segments. Montero-Serrano et al. (2015) considered TOC, P, As, V and Ni as proxies for reconstructing organic matter productivity. Based on their data, the succession deposited during the latter half of the isotopic segment J1 to about the early half of J2 was characterized by high primary productivity. Higher values in the C_{org}/P ratio, used by Remirez and Algeo (2020a) as a proxy for primary productivity, were observed over most of the Jenkyns Event, with greater values close to the top of J1. No indications on primary productivity based on elemental data are available for the Sancerre, Dotternhausen and Shandelah sections. Based on the available data, the correlation of Figure 12 suggests that, even if with a different extent from section to section, primary productivity increased (and peaked) close to the J1/J2 boundary. Moreover, sections from the shallow-water shelf regions in epicontinental northern Europe were characterized by higher organic matter fluxes compared to the Sogno and Peniche sections in the southern part of the northwestern portion of the Tethys.

Redox conditions varied substantially from section to section (Figure 12). The Dogna Core (Belluno Basin, Italy), drilled next to the Longarone section (Bellanca et al., 1999), was deposited under dysoxic to suboxic conditions, as indicated by variations in bioturbation intensity (Bellanca et al., 1999), Mo isotopes (Dickson et al., 2017), and molecular biomarker data (Farrimond et al., 1994). At Peniche, redox conditions were generally mild, with dysoxia starting to develop at the onset of the Jenkyns Event and continuing across the isotopic segment J2. This interpretation derives from the almost complete lack of benthic fauna and the presence of weakly bioturabated marls (Suan et al., 2008). Transient more reducing conditions (suboxic) occurred in correspondence of the 8-cm-thick black shale deposited during the lowest point in the trough of the Jenkyns Event as supported by redox-sensitive elemental data (Hermoso et al., 2009b; Fantasia et al., 2019a). The lack of bioturbation and redox-sensitive elements suggest that, at Creux de l'Ours, suboxic conditions dominated from the base of the Jenkyns Event up to the lower part of the J2 isotopic segment (Fantasia et al., 2018). In the overlying interval, the presence of bioturbation and lower concentrations in redox-sensitive elements probably record for a shift to more dysoxic conditions. At Bächental (Austria) redox conditions were reconstructed by Neumeister et al. (2015) based on Pr/Ph ratios, bioturbation, and Fe-TOC-S data. According to their data, suboxic conditions with possible short-term episodes of anoxia dominated for the earliest part of the Jenkyns Event, passing upward to strictly anoxic conditions that persisted up to the lowermost part of the J2 isotopic segment, and finally shifted back to less reducing suboxic to anoxic conditions. The presence of variable amounts of aryl isoprenoids probably indicates frequent but transient episodes of photic-zone euxinia in the upper part of the J1 isotopic segment (Neumeister et al., 2015). Based on molecular biomarkers, the black shale interval in the Réka Valley section (Hungary) was interpreted as deposited under anoxic conditions (Ruebsam et al., 2018). However, as indicated by peaks in isorenieratane, episodic extension of H_2S to near-surface waters occurred during the time of the lowest point in the carbon-isotope trough of the Jenkyns Event, approximately in correspondence with the central part of the J2 isotopic segment (Ruebsam et al., 2018). At Sancerre, the interval immediately below the black shales is characterized by grey marlstones with increased concentrations of redox-sensitive elements. However, as some bioturbation was observed in this part of the record (Hermoso et al., 2009b, 2013), we assume that conditions were dysoxic to suboxic. The black shale interval is, instead, completely devoid of benthic fauna. Furthermore, high concentrations of redox-sensitive elements (e.g., Fe/Al, Mn/Al, V/Al, and Mo), depletion in Mn and the presence of framboidal pyrite (on average about 5 μm in diameter) suggest that the sedimentation occurred under euxinic bottom waters that persisted from the middle J1 to the earliest J2 (Hermoso et al., 2009a, b, 2013). Following the interpretation proposed by Hermoso et al. (2009b), redox conditions then shifted to suboxic across the J2 interval before returning to fully oxic conditions shortly after the end of the Jenkyns Event. On the basis of elemental data (Fe, Cu, Zn and Co) and the lack of bioturbation, the laminated black shales of the Rietheim section were interpreted as deposited mostly under anoxic (possibly euxinic?) conditions (Montero-Serrano et al., 2015; Fantasia et al., 2018). Following their interpretation, euxinic conditions persisted for the entire Jenkyns Event and about half of the interval recording the positive excursion following the negative anomaly, shifting then to mainly suboxic conditions. The Dotternhausen succession documents a shift from fully oxic conditions to euxinic at the onset of the Jenkyns Event. Low oxygen levels are documented by the presence of distinct microlaminations and decrease followed by absence of benthic fauna (Röhl et al., 2001; Schwark and Frimmel, 2004; Röhl and Schmid-Röhl et al., 2005). Redox-sensitive elements, Mo-isotopes and Mo/TOC ratio suggest that euxinia persisted across the entire Jenkyns Event in a not fully restricted setting with some evidence of seawater renewal capable of bringing new oxygen to the basin (Dickson et al., 2017; Baroni et al., 2018; Wang et al., 2020). Euxinic conditions persisted also after the Jenkyns Event, even if with some evidence of temporary increase in the oxygenation state (Dickson et al., 2017). Evidence of photic-zone euxinia was reported on the basis of the presence of aryl-isoprenoids, chlorobactane, and isorenieratane peaking in concentration in correspondence with the most negative values of the Jenkyns Event (Schouten et al., 2000; Schwark and Frimmel, 2004). After the end of the Jenkyns Event photic-zone euxinia likely became seasonal (Schwark and Frimmel, 2004). Similar conditions were documented for the Schandelah Core, where the laminated black shales (Visentin et al., 2021) were interpreted, on the basis of redox-sensitive elemental data (i.e., Fe/Al, Mo, Mn, S, V, Cu), as deposited under anoxic conditions characterized by prolonged periods of euxinia interrupted by some brief oxygenation interludes (Baroni et al., 2018). Oxygenation conditions progressively improved after the end of the Jenkyns Event. The Yorkshire (UK) succession records suboxic conditions prior to the onset of the Jenkyns Event, with dark grey mudrocks characterized by a drastic reduction in bioturbation and type of trace fossils and body fossils (Caswell and Frid, 2017). Elemental data (including Mo, Re/Mo), Mo/TOC and Mo isotopes show that, due to highly stratified conditions, redox conditions shifted to intermittent euxinia at the onset of the Jenkyns Event (McArthur et al., 2008; Pearce et al., 2008; Dickson et al., 2017; Baroni et al., 2018; Thibault et al., 2018; McArthur, 2019; Houben et al., 2021). Euxinia persisted for the entire Jenkyns Event, interrupted by brief phases of re-oxygenation (McArthur et al., 2008; Baroni et al., 2018). Euxinic conditions continued also after the event but with progressively lower intensity. Bowden et al. (2006) and French et al. (2014) interpreted the presence of aryl-isoprenoids, okenane and chlorobactane within the black shale interval as evidence of photic-zone euxinia. However, French et al. (2014) argued that observed okenane, and potentially chlorobactane and isorenieratane, was most likely derived from mat-dwelling Chromatiaceae rather than marine sulphidic conditions.

The comparison of the available records allows us to draw some conclusions on the lateral and vertical evolution of redox conditions:

i) A shift to more reducing conditions started in all basins at the onset of the Jenkyns Event, even if some locations were characterized by dysoxic to suboxic conditions shortly before the beginning of the negative carbon-isotope anomaly;

ii) Reducing conditions became generally more severe close to the time indicated by the lowest point in the carbon-isotope trough of the Jenkyns Event;

iii) The Alpine-Mediterranean Tethys and the marginal proto-Atlantic were mainly dominated by dysoxic to suboxic conditions;

iv) Anoxia and transient euxinia occurred mainly on the shallow north European epicontinental shelf and, locally, in deeper nearby basins;

v) The recovery back to higher dissolved oxygen levels started earlier in the Alpine-Mediterraneann Tethys, while euxinia persisted for the entire Jenkyns Event and locally after it in the shallow-water basins and sub-basins of the north European epicontinental seaway.

With the exception of few isolated cases, deposition of black shales was mainly limited to northern shelf basins (Fig. 13). High TOC values (> 10 %) are common in this area, while most of the sections located elsewhere in the Alpine-Mediterranean Tethys generally present TOC contents < 2 % (Ruebsam et al., 2018; Remirez and Algeo, 2020b; Kemp et al., 2022; this study). Local water-column stratification induced by the input of brackish waters from the Arctic Ocean through the Viking Corridor (Dera and Donnadieu, 2012) or increased runoff from local landmasses (Cohen et al., 2004; McArthur et al., 2008; Bodin et al., 2010; Hermoso and Pellenard, 2014; Montero-Serrano et al., 2015; Fantasia et al., 2018; Remirez and Algeo, 2020a) has been invoked by many authors as the main cause of anoxia/euxinia in the northern shallow basins and sub-basins (Jenkyns, 1988; Suan et al., 2015; Fantasia et al., 2019a; McArthur, 2019; Remirez and Algeo, 2020b). The local presence of anoxia and transient photic-zone euxinia in deeper Alpine-Mediterranean Tethyan areas close to the northern epicontinental seaway has been explained either as the result of peculiar local basin physiography favorable to the onset of water-column stratification and deep-water anoxia (Neumeister et al., 2015), or as the result of an expanded oxygen minimum zone favored by an enhanced primary productivity and high organic-matter export rates (Ruebsam et al., 2018). Outside of this area, suboxia prevailed during the T-OAE in the Alpine-Mediterranean continental margin of the Tethys (Hermoso et al., 2009b; Bodin et al., 2010; Reolid et al., 2014a; Dickson et al., 2017; Fantasia et al., 2019a; Ruebsam et al., 2020a), with mild reducing conditions extending also into greater water depths.

6. CONCLUSIONS

The Sogno Core, due to its palaeowater depth of about 1500 m, represents one of the deepest records of the T-OAE in the Alpine-Mediterranean Tethys. Our data indicate that at the studied site no significant environmental change occurred at the onset of T-OAE and that conditions remained stable for most of the earliest part of the event. The climatic perturbation began only slightly before the onset of the negative carbon-isotope excursion of the Jenkyns Event as evidenced by oxygen-isotope ratios indicating a shift to warmer conditions coupled with enhanced weathering and detrital supply. With the onset of the Jenkyns Event a switch in the depositional style occurred as indicated by deposition of the Fish Level, that reached its maximum in correspondence with the most negative values of the Jenkyns Event. Together with the general increase in temperatures, a progressive intensification of runoff and nutrient supply favored relatively higher levels of primary productivity. The increase of riverine runoff induced a progressive lowering of surface-water salinity that, coupled with a steeper thermocline, may have favored the establishment of a stable pycnocline. We infer that vertical mixing became progressively less efficient, thereby favoring the establishment of more reducing bottom-water conditions that reached their relative maximum close to the interval of the most negative values of the Jenkyns Event. Dysoxic conditions, mainly limited to pore waters, developed initially during the earliest isotopic segment J1. Subsequently, suboxic bottom waters were established during the earliest part of the isotopic segment J2. With the progressive cooling that started in correspondence with the end of the isotopic segment J1, environmental conditions began to gradually recover: runoff intensity started to decline, as did primary productivity and detrital input. The end of the deposition of the Fish Level represents a return from suboxic to fully oxic bottom waters. During the earliest isotopic segment J2, after the deposition of the Fish Level, two discrete organic-rich black shales probably record short-lived pulses in runoff that due to enhanced stratification shifted deep waters back to more reducing conditions. Environmental conditions then remained stable up to the end of T-OAE and after with no changes coinciding with the end of the T-OAE.

Relatively shallow-water sites in the Alpine-Mediterranean Tethys including carbonate platforms, were generally characterized by milder reducing conditions with only limited and local areas characterized by anoxia. The deep-water redox conditions uniquely recorded in the Sogno Core document suboxic conditions, confirming that a lower oxygenation state prevailed in deep-water settings during the T-OAE in the Alpine-Mediterranean Tethys, in contrast to the widely documented anoxic and euxinic conditions that occurred in shallow water (15−150 m) shelf regions in the northern epicontinental basins and sub-basins and, locally, in deeper nearby basins.

ACKNOWLEDGMENTS

The research was conducted within the PRIN 2017RX9XXXY awarded to EE and the Italian Ministry of Education (MIUR) project “Dipartimenti di Eccellenza 2018–2022, Le Geoscienze per la Società: Risorse e loro evoluzione”. The authors are grateful to two anonymous Reviewers who, with their valuable comments, contributed greatly to improving the quality of the manuscript.

APPENDICES

Supplementary material A consists of a photograph of the rectangular-shaped mask used to carry out semi-quantitative visual analysis of pyrite and bioturbation distribution, and tables reporting average major and trace elements measured for different intervals along the Sogno Core.

Supplementary material B includes original data for bioturbation and pyrite distribution, XRF elemental concentrations, TOC/Rock Eval, and biomarker data.

REFERENCES

Aguilar-Islas, A., Bruland, K., 2006. Dissolved manganese and silicic acid in the Columbia River plume. Marine Chemistry, 101, 233–247, doi:10.1016/j.marchem.2006.03.005

Algeo, T.J., Maynard, J.B., 2004. Trace-element behavior and redox facies in core shales of Upper Pennsylvanian Kansas-type cyclothems. Chemical Geology, 206, 289–318. https://doi.org/10.1016/j.chemgeo.2003.12.009

Algeo, T.J., Tribovillard, N., 2009. Environmental analysis of paleoceanographic systems based on molybdenum–uranium covariation. Chemical Geology, 268, 211–225. https://doi.org/10.1016/j.chemgeo.2009.09.001

Algeo, T.J., Li, C., 2020. Redox classification and calibration of redox thresholds in sedimentary systems. Geochimica et Cosmochimica Acta, 287, 8–26. https://doi.org/10.1016/j.gca.2020.01.055

Algeo, T.J., Liu, J., 2020. A re-assessment of elemental proxies for paleoredox analysis. Chemical Geology, 540, 119549. https://doi.org/10.1016/j.chemgeo.2020.119549

Bacelle, L., Bosellini, A., 1965. Diagrammi per la stima visiva della composizione percentuale nelle rocce sedimentary. Annali dell'Università di Ferrara (Nuova Serie), Sezione 9, Scienze geologiche e paleontologiche, Vol. 1, No. 3, 59–62, 15 Pls.

Baroni, I.R., Pohl, A., van Helmond, N.A.G.M., Papadomanolaki, N.M., Coe, A.L., Cohen, A.S., van de Schootbrugge, B., Donnadieu, Y., Slomp, C.P., 2018. Ocean Circulation in the Toarcian (Early Jurassic): A Key Control on Deoxygenation and Carbon Burial on the European

Shelf. Paleoceanography and Paleoclimatology, 33, 994–1012. https://doi.org/10.1029/2018PA003394

Bailey, T.R., Rosenthal, Y., McArthur, J.M., Van De Schootbrugge, B., Thirlwall, M.F., 2003. Paleoceanographic changes of the late Pliensbachian–early Toarcian interval: a possible link to the genesis of an Oceanic Anoxic Event. Earth And Planetary Science Letters, 212, 307–320. https://doi.org/10.1016/S0012-821X(03)00278-4

Behar, F., Beaumont, V., Penteado, H.L. De B., 2001. Rock-Eval 6 Technology: performances and developments. Oil and gas Science and Technology – Revue de l'Institut Francais du Petrole, 56, 111–134. https://doi.org/10.2516/ogst:2001013

Bellanca, A., Masetti, D., Neri, R., Venezia, F., 1999. Geochemical and sedimentological evidence of productivity cycles recorded in Toarcian black shales from the Belluno Basin, Southern Alps, Northern Italy. Journal of Sedimentary Research, 69, 466–476. https://doi.org/10.2110/jsr.69.466

Bernoulli, D., Jenkyns, H.C., 1974. Alpine, Mediterranean, and Central Atlantic Mesozoic facies in relation to the early evolution of the Tethys. In R.H. Dott, R.H. Shaver (Eds.), Modern and Ancient Geosynclinal Sedimentation (Vol. 19, pp. 129–160). Houston, US: Society for Sedimentary Geology.

Bernoulli, D., Jenkyns, H.C., 2009. Ancient oceans and continental margins of the Alpine-Mediterranean Tethys: Deciphering clues from Mesozoic pelagic sediments and ophiolites. Sedimentology, 56, 149–190. https://doi.org/10.1111/j.1365-3091.2008.01017.x

Bjerrum, C.J., Surlyk, F., Callomon, J.H., Slingerland R.L., 2001. Numerical Paleoceanographic Study of the Early Jurassic Transcontinental Laurasian Seaway. Paleoceanography, 16, 390–404. https://doi.org/10.1029/2000PA000512

Bodin, S., Mattioli, E., Fröhlich, S., Marshall, J.D., Boutib, L., Lahsini, S., Redfern, J., 2010. Toarcian carbon isotope shifts and nutrient changes from the Northern margin of Gondwana (High Atlas, Morocco, Jurassic): Palaeoenvironmental implications. Palaeogeography, Palaeoclimatology, Palaeoecology, 297, 377–390. doi:10.1016/j.palaeo.2010.08.018

Bosence, D., Procter, E., Aurell, M., Kahla, A.B., Boudagher-Fadel, M., Casaglia, F., Cirilli, S., Mehdie, M., Nieto, L., Rey, J., Scherreiks, R., Soussi, M., Waltham, D., 2009. A Dominant Tectonic Signal in High-Frequency, Peritidal Carbonate Cycles? A Regional Analysis of Liassic Platforms from Western Tethys. Journal of Sedimentary Research, 79, 389–415. doi: 10.2110/jsr.2009.038

Bowden, A.S., Farrimond, P., Snape, C.E., Love, G.D., 2006. Compositional differences in biomarker constituents of the hydrocarbon, resin, asphaltene and kerogen fractions: An example from the Jet Rock (Yorkshire, UK). Organic Geochemistry, 37, 369–383. doi:10.1016/j.orggeochem.2005.08.024

Bray, E.E.., Evans, E.D., 1961. Distribution of n-paraffins as a clue to recognition of source beds. Geochimica et Cosmochimica Acta, 22, 2–15. https://doi.org/10.1016/0016-7037(61)90069-2

Bromley, R.G., 1990. Trace fossils. Biology and Taphonomy. Special Topics in Palaeontology Series. London, Boston, Sydney, Wellington: Unwin Hyman.

Bromley, R.G., Ekdale, A.A., 1984. Chondrites: a trace fossil indicator of anoxia in sediments. Science, 224, 872–874

Brumsack, H.-J., 1980. Geochemistry of Cretaceous black shales from the Atlantic Ocean (DSDP Legs 11, 14, 36 and 41). Chemical Geology, 31, 1–25. https://doi.org/10.1016/0009-2541(80)90064-9

Brumsack, H.-J., 1991. Inorganic geochemistry of the German 'Posidonia Shale': palaeoenvironmental consequences. In R.V. Tyson, T.H. Pearson (Eds.), Modern and Ancient Continental Shelf" Anoxia (Vol. 58, pp. 353–362). London, UK: Geological Society Special Publication. https://doi.org/10.1144/GSL.SP.1991.058.01.22

Brumsack, H.-J., 2006. The trace metal content of recent organic carbon-rich sediments: implications for Cretaceous black shale formation. Palaeogeography, Palaeoclimatology, Palaeoecology, 232, 344–361. https://doi.org/10.1016/j.palaeo.2005.05.011

Brazier, J.-M., Suan, G., Tacail, T., Simon, L., Martin, J.E., Mattioli, E., Balter, V., 2015. Calcium isotope evidence for dramatic increase of continental weathering during the Toarcian oceanic anoxic event (Early Jurassic). Earth and Planetary Science Letters, 411, 164–176. http://dx.doi.org/10.1016/j.epsl.2014.11.028

Calvert, S.E., Pedersen, T.F., 1993. Geochemistry of recent oxic and anoxic marine sediments: implications for the geological record. Marine Geology, 113, 67–88. https://doi.org/10.1016/0025-3227(93)90150-T

Calvert, S.E., Pedersen, T.F., 1996. Sedimentary geochemistory of manganese: implications for the environment of formation of manganiferous black shales. Economic Geology, 91, 36–47. https://doi.org/10.2113/gsecongeo.91.1.36

Calvert, S.E., Pedersen, T.F., 2007. Elemental proxies for palaeoclimatic and palaeoceanographic variability in marine sediments: interpretation and application. In C. Hillaire-Marcel, A. de Vernal (Eds.), Proxies in Late Cenozoic Paleoceanography (pp. 567–644). New York, NY: Elsevier.

Casellato, C.E., Erba, E., 2015. Calcareous nannofossil biostratigraphy and paleoceanography of the Toarcian Oceanic Anoxic Event at Colle di Sogno section (Southern

Alps, Italy). Rivista Italiana di Paleontologia e Stratigrafia, 105, 343–376. https://doi.org/10.13130/2039-4942/6520

Castellarin, A., 1972. Evoluzione paleotettonica sinsedimentariadel limite tra ‘Piattaforma Veneta’ e ‘Bacino Lombardo’, a nord di Riva del Garda. Giornale di Geologia, serie 2a, 38, 11–212.

Caswell, B.A., Frid, C.L.J., 2017. Marine ecosystem resilience during extreme deoxygenation: the Early Jurassic oceanic anoxic event. Oecologia, 183, 275–290. doi: 10.1007/s00442-016-3747-6

Chester, R., Jickells, T., 2012. Marine Geochemistry. NJ, USA:Wiley-Blackwell.

Clift, P.D., Hodges, K.V., Heslop, D., Hannigan, R., Van Long, H., Calves, G., 2008. Correlation of Himalayan exhumation rates and Asian monsoon intensity. Nature Geoscience, 1, 875–880. doi: 10.1038/ngeo351

Cohen, A.S., Coe, A.L., Harding, S.M., Schwark, L., 2004. Osmium isotope evidence for the regulation of atmospheric CO_2 by continental weathering. Geology, 32, 157–160. doi: 10.1130/G20158.1

Corbin, J.-C., Person, A., Jatzoura, A., Ferré, B., Renard, M., 2000. Manganese in Pelagic carbonates: indication of major Tectonic events during the geodynamic evolution of a passive continental margin (the Jurassic European Margin of the Tethys–Ligurian Sea). Palaeogeography, Palaeoclimatology, Palaeoecology, 156, 123–138. https://doi.org/10.1016/S0031-0182(99)00135-2

Cox, R., Lowe, D.R., Cullers, R.L., 1995. The influence of sediment recycling and basement composition on evolution of mudrock chemistry in the southwestern United States.

Geochimica et Cosmochimica Acta, 59, 2919–2940. https://doi.org/10.1016/0016-7037(95)00185-9

Crusius, J., Calvert, S., Pedersen, T., Sage, D., 1996. Rhenium and molybdenum enrichments in sediments as indicators of oxic, suboxic, and sulfidic conditions of deposition. Earth and Planetary Science Letters, 145, 65–78. https://doi.org/10.1016/S0012-821X(96)00204-X

Dahl, T.W., Chappaz, A., Hoek, J., McKenzie, C.J., Svane, S., Canfield, D.E., 2017. Evidence of molybdenum association with particulate organic matter under sulfidic conditions. Geobiology, 15, 311–323. https://doi.org/10.1111/gbi.12220

Dera, G., Donnadieu, Y., 2012. Modeling evidences for global warming, Arctic seawater freshening, and sluggish oceanic circulation during the Early Toarcian anoxic event. Paleoceanography, 27, PA2211. doi:10.1029/2012PA002283

Dera, G., Brigaud, B., Monna, F., Laffont, R., Pucéat, E., Deconinck, J.-F., Pellenard, P., Joachimski, M.M., and Durlet, C., 2011. Climatic ups and downs in a disturbed Jurassic world. Geology, 39, 215–218. https://doi.org/10.1130/G31579.1

Dickson, A.J., 2017. A molybdenum-isotope perspective on Phanerozoic deoxygenation events. Nature Geoscience, 10, 721–726. https://doi.org/10.1038/ngeo3028

Dickson, A.J., Leng, M.J., Maslin, M.A., Röhl, U., 2010. Oceanic, atmospheric and ice-sheet forcing of South East Atlantic Ocean productivity and South African monsoon intensity during MIS-12 to 10. Quaternary Science Reviews, 27–28, 3963–3947. https://doi.org/10.1016/j.quascirev.2010.09.014

Dickson, A.J., Gill, B.C., Ruhl, M., Jenkyns, H.C., Porcelli, D., Idiz, E., Lyons, T.W., van den Boorn, S.H.J.M., 2017. Molybdenum-isotope chemostratigraphy and paleoceanography of the

Toarcian Oceanic Anoxic Event (Early Jurassic). Paleoceanography, 32, 813–829, doi:10.1002/2016PA003048

Didyk, B.M., Simoneit, B.R.T., Brassell, S.C., Eglington, G., 1978. Organic geochemical indicators of paleoenvironmental conditions of sedimentation. Nature, 272, 216‒222. https://doi.org/10.1038/272216a0

Ebli, O., Vetö, I., Lobitzer, H., Sajgó, C., Demény, A., Hetényi, M., 1998. Primary productivity and early diagenesis in the Toarcian Tethys on the example of the Mn-rich black shales of the Sachrang Formation, Northern Calcareous Alps. Organic Geochemistry, 29, 1635–1647. https://doi.org/10.1016/S0146-6380(98)00069-2

Elderfield, H., 1976. Manganese fluxes to the oceans. Marine Chemistry, 4, 103‒132. https://doi.org/10.1016/0304-4203(76)90001-3

Erba, E., 2004. Calcareous nannofossils and Mesozoic oceanic anoxic events. Marine Micropaleontology, 52, 85–106. https://doi.org/10.1016/j.marmicro.2004.04.007

Erba, E., Casellato, C.E., 2010. Paleoceanografia del Giurassico nella Tetide occidentale: l'archivio geologico del Bacino Lombardo. Rendiconti dell'Istituto Lombardo. Accademia di Scienze e Lettere, Special Publication on "Una nuova Geologia per la Lombardia", 447, 115–140.

Erba, E., Bottini, C., Faucher, G., Gambacorta, G., Visentin, S., 2019a. The response of calcareous nannoplankton to Oceanic Anoxic Events: The Italian pelagic record. Bollettino della Società Paleontologica Italiana, 58, 51–71. doi: 10.4435/BSPI.2019.08

Erba, E., Gambacorta, G., Visentin, S., Cavalheiro, L., Reolon, D., Faucher, G., Pegoraro, M., 2019b. Coring the sedimentary expression of the early Toarcian Oceanic Anoxic Event: new stratigraphic records from the Tethys Ocean. Scientific Drilling, 26, 17‒27, 2019.

Erba, E., Cavalheiro, L., Dickson, A. J., Faucher, G., Gambacorta, G., Jenkyns, H. C., Wagner, T., 2022. Carbon- and oxygen-isotope signature of the Toarcian Oceanic Anoxic Event: insights from two Tethyan pelagic sequences (Gajum and Sogno Cores – Lombardy Basin, northern Italy). Newsletters on Stratigraphy, https://doi.org/10.1127/nos/2022/0690

Ettinger, N.P., Larson, T.E., Kerans, C., Thibodeau, A.M., Hattori, K.E., Kacur, S.M., Martindale, R.C., 2021. Ocean acidification and photic-zone anoxia at the Toarcian Oceanic Anoxic Event: Insights from the Adriatic Carbonate Platform. Sedimentology, 68, 63–107. https://doi.org/10.1111/sed.12786

Fantasia, A., Föllmi, K.B., Adatte, T., Spangenberg, J.E., Montero-Serrano, J.-C., 2018. The Early Toarcian oceanic anoxic event: Paleoenvironmental and paleoclimatic change across the Alpine Tethys (Switzerland). Global and Planetary Change, 162, 53–68. https://doi.org/10.1016/j.gloplacha.2018.01.008

Fantasia, A., Adatte, T., Spangenberg, J.E., Font, E., Duarte, L.V., Föllmi, K.B., 2019a. Global versus local processes during the Pliensbachian–Toarcian transition at the Peniche GSSP, Portugal: A multi-proxy record. Earth-Science Reviews, 198, 102932. https://doi.org/10.1016/j.earscirev.2019.102932

Fantasia, A., Föllmi, K.B., Adatte, T., Spangenberg, J.E., Mattioli, E., 2019b. Expression of the Toarcian Oceanic Anoxic Event: New insights from a Swiss transect. Sedimentology 66, 262–284.

Farrimond, P., Stoddart, D.P., Jenkyns, H.C., 1994. An organic geochemical profile of the Toarcian anoxic event in northern Italy. Chemical Geology 111, 17–33.

Farrimond, P., Taylor, A., Telnæs, N., 1998. Biomarker maturity parameters: the role of generation and thermal degradation. Organic Geochemistry, 29, 1181–1197. https://doi.org/10.1016/S0146-6380(98)00079-5

Faucher, G., Visentin, S., Gambacorta, G., Erba, E., 2022. *Schizosphaerella* size and abundance variations across the Toarcian Oceanic Anoxic Event in the Sogno Core (Lombardy Basin, Southern Alps). Palaeogeography, Palaeoclimatology, Palaeoecology, 595, 110969. https://doi.org/10.1016/j.palaeo.2022.110969

Font, E., Duarte, L.V., Dekkers, M.J., Remazeilles, C., Egli, R., Spangenberg, J.E., Fantasia, A., Ribeiro, J., Gomes, E., Mirão, J., Adatte T., 2022. Rapid light carbon releases and increased aridity linked to Karoo–Ferrar magmatism during the early Toarcian oceanic anoxic event. Scientific Reports, 12, 4342. https://doi.org/10.1038/s41598-022-08269-y

Fraguas, À., Gómez, J.J., Goy, A., Comas-Rengifo, M.J., 2021. The response of calcareous nannoplankton to the latest Pliensbachian–early Toarcian environmental changes in the Camino Section (Basque Cantabrian Basin, northern Spain). In M. Reolid, L.V. Duarte, E. Mattioli, W. Ruebsam (Eds.), Carbon Cycle and Ecosystem Response to the Jenkyns Event in the Early Toarcian (Jurassic) (Vol. 514, pp. 31 – 58). London, UK: Geological Society Special Publication. https://doi.org/10.1144/SP514-2020-256

French, K.L., Sepúlveda, J., Trabucho-Alexandre, J., Gröcke, D.R., Summons, R.E., 2014. Organic geochemistry of the early Toarcian oceanic anoxic event in Hawsker Bottoms, Yorkshire, England. Earth and Planetary Science Letters, 390, 116–127. http://dx.doi.org/10.1016/j.epsl.2013.12.033

Gaetani, M., 1975. Jurassic stratigraphy of the Southern Alps: a review. In: Squyres, C. H. (Ed.), Geology of Italy (Vol. I, pp. 377–402). Tripoli, Libya, Earth Sciences Society of the Libyan

Arab Republic.

Gaetani, M., 2010. From Permian to Cretaceous: Adria as pivotal between extensions and rotations of Tethys and Atlantic Oceans. In M. Beltrando, A. Peccerillo, M. Mattei, S. Conticelli, C. Doglioni (Eds.), The Geology of Italy. Journal of the Virtual Explorer 36, paper 5.a, https://doi.org/10.3809/jvirtex.2010.00235, 2010

Gaetani, M., Erba, E., 1990. Il bacino Lombardo: un sistema paleoalto/fossa in un margine continentale passivo durante il Giurassico. Guida all'escursione A3. Paper presented at 75° Congresso Società Geologica Italiana, 10–12 September 1990, Milano, Italy.

Gaetani, M., Poliani, G., 1978. Il Toarciano e il Giurassico medio in Albenza (Bergamo). Rivista Italiana di Paleontologia e Stratigrafia, 84, 349–382.

Ganeshram, R.S., Calvert, S.E., Pedersen, T.F., Cowie, G.L., 1999. Factors controlling the burial of organic carbon in laminated and bioturbated sediments off NW Mexico: implications for hydrocarbon preservation. Geochimica et Cosmochimica Acta, 63, 1723–1734. https://doi.org/10.1016/S0016-7037(99)00073-3

Gómez, J.J., Comas-Rengifo, M.J., Goy, A., 2016. Palaeoclimatic oscillations in the Pliensbachian (Early Jurassic) of the Asturian Basin (Northern Spain). Climate of the Past, 12, 1199–1214. https://doi.org/10.5194/cp-12-1199-2016

Hallam, A., 1981. A revised sea-level curve for the early Jurassic. Journal of the Geological Society, 138, 735–743. https://doi.org/10.1144/gsjgs.138.6.0735

Haq, B.U., Hardenbol, J., Vail, P.R., 1987. Chronology of fluctuating sea-levels since the Triassic. Nature, 235, 1156–1167. doi: 10.1126/science.235.4793.1156

Hardenbol, J., Thierry, J., Farley, M.B., Jacquin, T., de Graciansky, P.-C., Vail, P.R., 1998. Mesozoic and Cenozoic sequence chronostratigraphic framework of European basins. In P.-C. de

Graciansky, J. Hardenbol, T. Jacquin, P.R. Vail (Eds.), Mesozoic and Cenozoic sequence stratigraphy of European basins (Vol. 60, pp. 3‒13). Tulsa, Oklahoma: Society for Sedimentary Geology.

Heimdal, T.H., Goddéries, Y., Jones, M.T., Svensen, H.H., 2021. Assessing the importance of thermogenic degassing from the Karoo Large Igneous Province (LIP) in driving Toarcian carbon cycle perturbations. Nature Communications, 12, doi: 10.1038/s41467-021-26467-6.

Heinrichs, H., Schulz-Dobrick, B., Wedepohl, K.H., 1980. Terrestrial geochemistry of Cd, Bi, Tl, Pb, Zn and Rb. Geochimica et Cosmochimica Acta, 44, 1519–1533. https://doi.org/10.1016/0016-7037(80)90116-7

Hermoso, M., Pellenard, P., 2014. Continental weathering and climatic changes inferred from clay mineralogy and paired carbon isotopes across the early to middle Toarcian in the Paris Basin. Palaeogeography, Palaeoclimatology, Palaeoecology, 399, 385‒393. http://dx.doi.org/10.1016/j.palaeo.2014.02.007

Hermoso, M., Le Callonnec, L., Minoletti, F., Renard, M., Hesselbo, S., 2009a. Expression of the Early Toarcian negative carbon-isotope excursion in separated carbonate microfractions (Jurassic, Paris Basin). Earth and Planetary Science Letters, 277, 194‒203. doi:10.1016/j.epsl.2008.10.013

Hermoso, M., Minoletti, F., Le Callonnec, L., Jenkyns, H.C., Hesselbo, S.P., Rickaby, R.E. M., Renard, M., de Rafélis, M., Emmanuel, L., 2009b. Global and local forcing of Early Toarcian seawater chemistry: A comparative study of different paleoceanographic settings (Paris and Lusitanian basins). Paleoceanography, 24, PA4208, doi:10.1029/2009PA001764.

Hermoso, M., Minoletti, F., Rickaby, R.E.M., Hesselbo, S.P., Baudin, F., Jenkyns, H.C., 2012. Dynamics of a stepped carbon-isotope excursion: Ultra high-resolution study of Early

Toarcian environmental change. Earth and Planetary Science Letters, 319–320, 45–54. doi:10.1016/j.epsl.2011.12.021

Hermoso, M., Minoletti, F., Pellenard, P., 2013. Black shale deposition during Toarcian super-greenhouse driven by sea level. Climate of the Past, 9, 2703–2712. doi:10.5194/cp-9-2703-2013

Hesselbo, S.P., 2008. Sequence stratigraphy and inferred relative sea-level change from the onshore British Jurassic. Proceedings of the Geologists' Association, 119, 19–34. https://doi.org/10.1016/S0016-7878(59)80069-9

Hesselbo, S.P., Gröcke, D.R., Jenkyns, H.C., Bjerrum, C.J., Farrimond, P., Morgans Bell, H. S., Green, O.R., 2000. Massive dissociation of gas hydrate during a Jurassic Oceanic Anoxic Event. Nature, 406, 392–395. doi: 10.1038/35019044

Hesselbo, S.P., Jenkyns, H.C., Duarte, L.V., Oliveira, L.C.V., 2007. Carbon-isotope record of the Early Jurassic (Toarcian) Oceanic Anoxic Event from fossil wood and marine carbonate (Lusitanian Basin, Portugal). Earth and Planetary Science Letters, 253, 455–470. doi:10.1016/j.epsl.2006.11.009

Hild, E., Brumsack, H.-J., 1998. Major and minor element geochemistry of Lower Aptian sediments from the NW German Basin (core Hoheneggelsen KB 40). Cretaceous Research, 19, 615–633. https://doi.org/10.1006/cres.1998.0122

Houben, A.J.P., Goldberg, T., Slomp, C.P., 2021. Biogeochemical evolution and organic carbon deposition on the Northwestern European Shelf during the Toarcian Ocean Anoxic Event. Palaeogeography, Palaeoclimatology, Palaeoecology, 565, 110191. https://doi.org/10.1016/j.palaeo.2020.110191

Hu, X., Cheng, W., Ji, J., 2009. Origin of Cretaceous Oceanic Red Beds from the Vispi

Quarry Section, Central Italy: Visible Reflectance and Inorganic Geochemistry. In X. Hu, C. Wang, R.W. Scott, M. Wagreich, L. Jansa (Eds.), Cretaceous Oceanic Red Beds: Stratigraphy, Composition, Origins, and Paleoceanographic and Paleoclimatic Significance (Vol. 91, pp. 183–199). Houston, US: Society for Sedimentary Geology.

Huerta-Diaz, M.A., Morse, J.W., 1990. A quantitative method for determination of trace metal concentrations in sedimentary pyrite. Marine Chemistry, 29, 119–144. https://doi.org/10.1016/0304-4203(90)90009-2

Huerta-Diaz, M.A., Morse, J.W., 1992. Pyritisation of trace metals in anoxic marine sediments. Geochimica et Cosmochimica Acta, 56, 2681–2702. https://doi.org/10.1016/0016-7037(92)90353-K

Izumi, K., Kemp, D.B., Itamiya, S., Inui, M., 2018. Sedimentary evidence for enhanced hydrological cycling in response to rapid carbon release during the early Toarcian oceanic anoxic event. Earth and Planetary Science Letters, 481, 162–170. https://doi.org/10.1016/j.epsl.2017.10.030

Jenkyns, H.C., 1985. The Early Toarcian and Cenomanian-Turonian anoxic events in Europe: comparisons and contrasts. Geologische Rundschau, 74, 505–518.

Jenkyns, H.C., 1988. The Early Toarcian (Jurassic) Anoxic Event: stratigraphic, sedimentary and geochemical evidence. American Journal of Science, 288, 101–151.

Jenkyns, H.C., 2003. Evidence for rapid climate change in the Mesozoic–Palaeogene greenhouse world. Philosophical Transactions of the Royal Society of London, Series A, 361, 1885–1916. https://doi.org/10.1098/rsta.2003.1240

Jenkyns, H.C., 2010. Geochemistry of oceanic anoxic events. Geochemistry, Geophysics, Geosystems, 11, Q03004, doi: 10.1029/2009GC002788.

Jenkyns, H. C., 2020. The demise and drowning of Early Jurassic (Sinemurian) carbonate platforms: stratigraphic evidence from the Italian peninsula, Sicily and Spain. In: l'eredità scientifica di Paolo Scandone, geologo, Atti dei Convegni Lincei, Roma 335, 55–83.

Jenkyns, H. C., Clayton, C. J., 1986. Black shales and carbon isotopes in pelagic sediments from the Tethyan Lower Jurassic. Sedimentology 33, 87–106.

Jenkyns, H.C., Clayton, C.J., 1997. Lower Jurassic epicontinental carbonates and mudstones from England and Wales: chemostratigraphic signals and the early Toarcian anoxic event. Sedimentology, 44, 687–706. doi: 10.1046/j.1365-3091.1997.d01-43.x

Jenkyns, H.C., Géczy, B., Marshall, J.D., 1991. Jurassic manganese carbonates of Central Europe and the early Toarcian Anoxic Event. The Journal of Geology, 99, 137–149.

Jenkyns, H.C., Gröcke, D.R., Hesselbo, S.P., 2001. Nitrogen isotope evidence for water mass denitrification during the early Toarcian (Jurassic) oceanic anoxic event. Paleoceanography, 16, 593–603. https://doi.org/10.1029/2000PA000558

Jenkyns, H.C., MacFarlane, S., 2021. The chemostratigraphy and environmental significance of the Marlstone and Junction Bed (Beacon Limestone, Toarcian, Lower Jurassic, Dorset, UK). Geological Magazine, 159, 357–371. doi: 10.1017/S0016756821000972.

Kemp, D.B., Coe, A.L., Cohen, A.S., Schwark, L., 2005. Astronomical pacing of methane release in the Early Jurassic period. Nature, 437, 396–399. doi:10.1038/nature04037

Kemp, D.B., Selby, D., Izumi, K., 2020. Direct coupling between carbon release and weathering during the Toarcian oceanic anoxic event. Geology, 48, 976–980. https://doi.org/10.1130/G47509.1

Kemp, D.B., Chen, W., Cho, T., Algeo, T.J., Shen, J., Ikeda, M., 2022. Deep-ocean anoxia across the Pliensbachian-Toarcian boundary and the Toarcian Oceanic Anoxic Event in the

Panthalassic Ocean. Global and Planetary Change, 212, 03782. https://doi.org/10.1016/j.gloplacha.2022.103782

Koopmans, M.P., Schouten, S., Kohnen, M.E.L., Sinnighe Damsté, J.S., 1996. Restricted utility of aryl isoprenoids as indicators for photic zone anoxia. Geochimica et Cosmochimica Acta, 60, 4873–4876. https://doi.org/10.1016/S0016-7037(96)00303-1

Korte, C., Hesselbo, S.P., 2011. Shallow marine carbon and oxygen isotope and elemental records indicate icehouse-greenhouse cycles during the early Jurassic. Paleoceanography, 26, PA4219, doi: 10.1029/2011PA002160.

Krencker, F.-N., Bodin, S., Suan, G., Heimhofer, U., Kabiri, L., Immenhauser, 2015. Toarcian extreme warmth led to tropical cyclone intensification. Earth and Planetary Science Letters, 425, 120–130. http://dx.doi.org/10.1016/j.epsl.2015.06.003

Large, D.J., Gize, A.P., 1996. Pristane/phytane ratios in the mineralized Kupferschiefer of the Fore-Sudetic Monocline, southwest Poland. Ore Geology Reviews, 11, 89–103. https://doi.org/10.1016/0169-1368(95)00017-8

Lézin, C., Andreu, B., Pellenard, P., Bouchez, J.-L., Emmanuel, L., Fauré, P., Landrein, P., 2013. Geochemical disturbance and paleoenvironmental changes during the Early Toarcian in NW Europe. Chemical Geology, 341, 1–15. http://dx.doi.org/10.1016/j.chemgeo.2013.01.003

Little, S.H., Vance, D., Lyons, T.W., McManus, J., 2015. Controls on trace metal authigenic enrichment in reducing sediments: insights from modern oxygen-deficient settings. American Journal of Science, 315, 77–119. https://doi.org/10.2475/02.2015.01

Lu, Z., Jenkyns, H.C., Rickaby, R.E., 2010. Iodine to calcium ratios in marine carbonate as a paleo-redox proxy during oceanic anoxic events. Geology, 38, 1107–1110. https://doi.org/10.1130/G31145.1

Lyons, T.W., Severmann, S., 2006. A critical look at iron paleoredox proxies: new insights from modern euxinic marine basins. Geochimica et Cosmochimica Acta, 70, 5698–5722. https://doi.org/10.1016/j.gca.2006.08.021

Mattioli, E., Pittet, B., Bucefalo Palliani, R., Röhl, H.-J., Schmid-Röhl, A., Morettini, E., 2004. Phytoplankton evidence for timing and correlation of palaeoceanographical changes during the Early Toarcian oceanic anoxic event (Early Jurassic). Journal of the Geological Society of London, 161, 685–693. https://doi.org/10.1144/0016-764903-074

McArthur, J.M., 2019. Early Toarcian black shales: A response to an oceanic anoxic event or anoxia in marginal basins? Chemical Geology, 522, 71‒83. https://doi.org/10.1016/j.chemgeo.2019.05.028

McArthur, J.M., Algeo, T.J., van de Schootbrugge, B., Li, Q., Howarth, R.J., 2008. Basinal restriction, black shales, Re-Os dating, and the Early Toarcian (Jurassic) oceanic anoxic event. Paleoceanography, 23, PA4217. doi:10.1029/2008PA001607

McElwain, J.C., Wade-Murphy, J., Hesselbo, S.P., 2005. Changes in carbon dioxide during an oceanic anoxic event linked to intrusion into Gondwana coals. Nature, 435, 479–482. doi: 10.1038/nature03618

Meinhardt, A.-K., Pahnke, K., Böning, P., Schnetger, B., Brumsack, H.-J., 2016. Climate change and response in bottom water circulation and sediment provenance in the Central Arctic Ocean since the Last Glacial. Chemical Geology, 427, 98‒108. http://dx.doi.org/10.1016/j.chemgeo.2016.02.019

Montero-Serrano, J.C., Föllmi, K.B., Adatte, T., Spangenberg, J.E., Tribovillard, N., Fantasia, A., Suan, G., 2015. Continental weathering and redox conditions during the early Toarcian Oceanic Anoxic Event in the northwestern Tethys: Insight from the Posidonia Shale section in the Swiss Jura Mountains. Paleogeography, Paleoclimatology, Paleoecology, 429, 83–99. http://dx.doi.org/10.1016/j.palaeo.2015.03.043

Morse, J.W., Luther III, G.W., 1999. Chemical influences on trace metal–sulfide interactions in anoxic sediments. Geochimica et Cosmochimica Acta, 63, 3373–3378. https://doi.org/10.1016/S0016-7037(99)00258-6

Müller, T., Price, G.D., Bajnai, D., Nyerges, A., Kesjár, D., Raucsik, B., Varga, A., Judik, K., Fekete, J., May, Z., Pálfy, J., 2017. New multiproxy record of the Jenkyns Event (also known as the Toarcian Oceanic Anoxic Event) from the Mecsek Mountains (Hungary): Differences, duration and drivers. Sedimentology 64, 66–86.

Müller, T., Jurikova, H., Gutjahr, M., Tomašovych, A., Schlögl, J., Liebetrau, V., Duarte, L. V., Milovský, R., Suan, G., Mattioli, E., Pittet, B., Eisenhauer, A., 2020a. Ocean acidification during the early Toarcian extinction event: Evidence from boron isotopes in brachiopods. Geology, 48, 1184–1188. https://doi.org/10.1130/G47781.1

Müller, T., Karancz, S., Mattioli, E., Milovský, R., Pálfy, J., Schlögl, J., Segit, T., Šimo, V., Tomašových, A., 2020b. Assessing anoxia, recovery and carbonate production setback in a hemipelagic Tethyan basin during the Toarcian Oceanic Anoxic Event (Western Carpathians). Global and Planetary Change, 103366.

Müller, T., Price, G.D., Mattioli, E., Leskó, M.Z., Kristály, F., Pálfy, J., 2021. Hardground, gap and thin black shale: spatial heterogeneity of arrested carbonate sedimentation during the Jenkyns Event (T-OAE) in a Tethyan pelagic basin (Gerecse Mts, Hungary). Geological Society, London, Special Publications 514, 269-289.

Neubert, N., Nägler, T.F., Böttcher, M.E., 2008. Sulphidity controls molybdenum isotope fractionation into euxinic sediments: Evidence from the modern Black Sea, Geology, 36, 775–778. https://doi.org/10.1130/G24959A.1

Neumeister, S., Gratzer, R., Algeo, T.J., Bechtel, A., Gawlick, H.J., Newton, R.J., Sachsenhofer, R.F., 2015. Oceanic response to Pliensbachian and Toarcian magmatic events: implications from an organic-rich basinal succession in the NW Tethys. Global and Planetary Change, 126, pp.62-83. https://doi.org/10.1016/j.gloplacha.2015.01.007

Pálfy, J., Smith, P.L., 2000. Synchrony between Early Jurassic extinction, oceanic anoxic event, and the Karoo-Ferrar flood basalt volcanism. Geology, 28, 747–750. https://doi.org/10.1130/0091-7613(2000)28<747:SBEJEO>2.0.CO;2

Pasquini, C., Vercesi, P.L., 2002. Tettonica sinsedimentaria e ricostruzione paleogeografica del margine occidentale dell'Alto dei Corni di Canzo nel Lias inferiore. Memorie della Società Geologica Italiana, 57, 107–114.

Pearce, C.R., Cohen, A.S., Coe, A.L., Burton, K.W., 2008. Molybdenum isotope evidence for global ocean anoxia coupled with perturbations to the carbon cycle during the Early Jurassic. Geology, 36, 231–234. https://doi.org/10.1130/G24446A.1

Percival, L.M.E., Witt, M.L.I., Mather, T.A., Hermoso, M., Jenkyns, H.C., Hesselbo, S.P., Al-Suwaidi, A.H., Storm, M.S., Xu, W., Ruhl, M., 2015. Globally enhanced mercury deposition during the end-Pliensbachian extinction and Toarcian OAE: A link to the Karoo–Ferrar Large Igneous Province. Earth and Planetary Science Letters, 428, 267–280. https://doi.org/10.1016/j.epsl.2015.06.064

Percival, L.M.E., Cohen, A.S., Davies, M.K., Dickson, A.J., Hesselbo, S.P., Jenkyns, H.C., Leng, M.J., Mather, T.A., Storm, M.S., Xu, W., 2016. Osmium isotope evidence for two pulses of increased continental weathering linked to Early Jurassic volcanism and climate change. Geology, 44, 759–762. https://doi.org/10.1130/G37997.1

Peters, K.E., Walters, C.C., Moldowan, J.M., 2005. The biomarker guide, Second Edition, Biomarkers and isotopes in the environment and human history. (Vol. I). New York, NY: Cambridge University Press.

Peti, L., Thibault, N., Korte, C., Ullmann, C.V., Cachão, M., Fibæk, M., 2021. Environmental drivers of size changes in lower Jurassic Schizosphaerella spp. Marine Micropaleontology, 168, 102053. https://doi.org/10.1016/j.marmicro.2021.102053

Pieńkowski, G., Hodbod, M., Ullmann, C.V., 2016. Fungal decomposition of terrestrial organic matter accelerated Early Jurassic climate warming. Scientific Reports, 6, 31930. doi: 10.1038/srep31930

Piper, D.Z., Calvert, S.E., 2009. A marine biogeochemical perspective on black shale deposition. Earth-Science Reviews, 95, 63–96. https://doi.org/10.1016/j.earscirev.2009.03.001

Polgári, M., Okita, P.M., Hein, J.R., 1991. Stable isotope evidence for the origin of the Urkut manganese ore deposit, Hungary. Journal of Sedimentary Research, 61, 384–393. https://doi.org/10.1306/D426771C-2B26-11D7-8648000102C1865D

Polgári, M., Hein, J.R., Vigh, T., Szabó-Drubina, M., Fórizs, I., Bíró, L., Müller, A., Tóth, L., 2012a. Microbial processes and the origin of the Úrkút manganese deposit. Hungary. Ore Geology Reviews, 47, 87–109.

Polgári, M., Hein, J.R., Tóth, A.L., Pál-Molnár, E., Vígh, T., Bíró, L., Fintor, K., 2012b. Microbial action formed JurassicMn-carbonate ore deposit in only a few hundred years (Úrkút, Hungary). Geology, 40, 903–906.

Polgári, M., Hein, J.R., Bíró, L., Gyollai, I., Németh, T., Sajgó, C., Fekete, J., Schwark, L., Pál-Molnár, E., Hámor-Vidó, M., Vigh, T., 2016. Mineral and chemostratigraphy of a Toarcian black shale hosting Mn-carbonate microbialites (Úrkút, Hungary). Palaeogeography, Palaeoclimatology, Palaeoecology, 459, 99–120.

Posenato, R., Bassi, D., Trecalli, A., Parente, M., 2018. Taphonomy and evolution of Lower Jurassic lithiotid bivalve accumulations in the Apennine Carbonate Platform (southern Italy). Palaeogeography, Palaeoclimatology, Palaeoecology, 489, 261–271. https://doi.org/10.1016/j.palaeo.2017.10.017

Potter, P.E., Maynard, J.B., Depetris, P.J., 2005. Mud and Mudstones: Introduction and Overview. Berlin-Heidelberg-New York: Springer.

Rachold, V, Brumsack, H.-J., 2001. Inorganic geochemistry of Albian sediments from the Lower Saxony Basin NW Germany: palaeoenvironmental constraints and orbital cycles. Palaeogeography, Palaeoclimatology, Palaeoecology, 174, 121–143. https://doi.org/10.1016/S0031-0182(01)00290-5

Remirez, M.N., Algeo, T.J., 2020a. Paleosalinity determination in ancient epicontinental seas: A case study of the T-OAE in the Cleveland Basin (UK). Earth Science Reviews, 201, 103072. https://doi.org/10.1016/j.earscirev.2019.103072

Remirez, M.N., Algeo, T.J., 2020b. Carbon-cycle changes during the Toarcian (Early Jurassic) and implications for regional versus global drivers of the Toarcian oceanic anoxic event. Earth-Science Reviews, 209, 103283. https://doi.org/10.1016/j.earscirev.2020.103283

Reolid, M., Rodríguez-Tovar, F.J., Marok, A., Sebane, A., 2012. The Toarcian oceanic anoxic event in the Western Saharan Atlas, Algeria (North African paleomargin): Role of anoxia and productivity. Geological Society of America Bulletin, 124, 1646–1664; doi:10.1130/B30585.1

Reolid, M., Mattioli, E., Nieto, L.M., Rodríguez-Tovar, F.J., 2014. The Early Toarcian Oceanic Anoxic Event in the External Subbetic (Southiberian Palaeomargin, Westernmost Tethys): Geochemistry, nannofossils and ichnology. Palaeogeography, Palaeoclimatology, Palaeoecology, 411, 79–94. http://dx.doi.org/10.1016/j.palaeo.2014.06.023

Reolid, M., Mattioli, E., Duarte, L.V., Marok, A., 2020. The Toarcian Oceanic Anoxic Event and the Jenkyns Event (IGCP-655 final report). Episodes, 43, 833–844. https://doi.org/10.18814/epiiugs/2020/020051

Reolid, M., Mattioli, E., Duarte, L.V., Ruebsam, W., 2021. The Toarcian Oceanic Anoxic Event: where do we stand? In: Reolid, M., Duarte, L.V., Mattioli, E., Ruebsam, W. (Eds), Carbon Cycle and Ecosystem Response to the Jenkyns Event in the Early Toarcian (Jurassic). Geological Society, London, Special Publications 514, 1–11.

Rodrigues, B., Duarte, L.V., Mendonca, J.G., Santos, L.G., de Oliveira, A.D., 2016. Evidence of terrestrial organic matter deposition across the early Toarcian recorded in the northern Lusitanian Basin Portugal. International Journal of Coal Geology, 168, 35–45. https://doi.org/10.1016/j.coal.2016.06.016

Rodriguez-Tovar, F.J., Reolid, M., 2013. Environmental conditions during the Toarcian Oceanic Anoxic Event (T-OAE) in the westernmost Tethys: influence of the regional context on a global phenomenon. Bulletin of Geosciences, 88, 697–712. doi: 10.3140/bull.geosci.1397

Röhl, H.-J., Schmid-Röhl, A., 2005. Lower Toarcian (Upper Liassic) black shales of the central european epicontinental basin: a sequence stratigraphic case study from the SW German Posidonia Shale. In N. B. Harris (Ed.), The Deposition of Organic-Carbon-Rich Sediments: Models, Mechanisms, and Consequences (Vol. 82, pp. 165–189). Houston, US: Society for Sedimentary Geology.

Röhl, H.-J., Schmid-Röhl, A., Oschmann, W., Frimmel, A., Schwark, L., 2001. The Posidonia Shale (Lower Toarcian) of SW-Germany: an oxygen-depleted ecosystem controlled by sea level and palaeoclimate. Palaeoceanography, Palaeoclimatology, Palaeoecology, 165, 27–52. https://doi.org/10.1016/S0031-0182(00)00152-8

Rothwell, R.G., Hoogakker, B., Thomson, J., Croudace, I.W., Frenz, M., 2006. Turbidite emplacement on the southern Balearic Abyssal Plain (western Mediterranean Sea) during Marine Isotope Stages 1–3: an application of ITRAX XRF scanning of sediment cores to lithostratigraphic analysis. In R. G. Rothwell (Ed.), New tecniques in sediment core analysis (Vol. 267, pp. 79 – 98). London, UK: Geological Society Special Publication.

Ruebsam, W., Müller, T., Kovács, J., Pálfy, J., Schwark, L., 2018. Environmental response to the early Toarcian carbon cycle and climate perturbations in the northeastern part of the West Tethys shelf. Gondwana Research, 59, 144–158.

Ruebsam, W., Mayer, B., Schwark, L., 2019. Cryosphere carbon dynamics control early Toarcian global warming and sea level evolution. Global and Planetary Change, 172, 440–453. https://doi.org/10.1016/j.gloplacha.2018.11.003

Ruebsam, W., Reolid, M., Marok, A., Schwark, L., 2020a. Drivers of benthic extinction during the early Toarcian (Early Jurassic) at the northern Gondwana paleomargin: Implications for paleoceanographic conditions. Earth-Science Reviews, 203, 103117. https://doi.org/10.1016/j.earscirev.2020.103117

Ruebsam, W., Reolid, M., Sabatino, N., Masetti, D., Schwark, L., 2020b. Molecular paleothermometry of the early Toarcian climate perturbation. Global and Planetary Change, 195, 103351. https://doi.org/10.1016/j.gloplacha.2020.103351

Ruhl, M., Hesselbo, S.P., Hinnov, L., Jenkyns, H.C., Xu, W., Riding, J.B., Storm, M., Minisini, D., Ullmann, C.V., Leng, M.J., 2016. Astronomical constraints on the duration of the Early JurassicPliensbachianStage and global climatic fluctuations. Earth and Planetary Science Letters, 455, 149–165.

Sabatino, N., Neri, R., Bellanca, A., Jenkyns, H.C., Baudin, F., Parisi, G., Masetti, D., 2009. Carbon-isotope records of the Early Jurassic (Toarcian) oceanic anoxic event from the Valdorbia (Umbria-Marche Apennines) and Monte Mangart (Julian Alps) sections: palaeoceanographic and stratigraphic implications. Sedimentology, 56, 1307–1328. https://doi.org/10.1111/j.1365-3091.2008.01035.x

Sabatino, N., Neri, R., Bellanca, A., Jenkyns, H.C., Masetti, D., Scopelliti, G., 2011. Petrography and high-resolution geochemical records of Lower Jurassic manganese-rich deposits from Monte Mangart, Julian Alps. Palaeoceanography, Palaeoclimatology, Palaeoecology, 299, 97–109. https://doi.org/10.1016/j.palaeo.2010.10.039

Sabatino, N., Vlahović, I., Jenkyns, H.C., Scopelliti, G., Neri, R., Prtoljan, B. Velić, I., 2013. Carbon-isotope record and palaeoenvironmental changes during the early Toarcian oceanic anoxic event in shallow-marine carbonates of the Adriatic Carbonate Platform in Croatia. Geological Magazine, 150, 1085–1102. https://doi.org/10.1017/S0016756813000083

Sageman, B.B., Lyons, T.W., 2005. Geochemistry of fine-grained sediments and sedimentary rocks. In H.D. Holland H.D., K. K. Turekian (Eds.), Sediments, Diagenesis, and Sedimentary Rocks – Treatise on Geochemistry (Vol. 7, 115–158). Elsevier, Amsterdam, Holland: Elsevier.

Santantonio, M., Carminati, E., 2011. The Jurassic rifting evolution of the Apennines and Southern Alps (Italy): Parallels and differences. Bulletin of the Geological Society of America, 124, 468–484. https://doi.org/10.1130/B30104.1

Schmitz, B., Charisi, S.D., Thompson, E.I., Speijer, R.P., 1997. Barium, SiO_2 (excess), and P_2O_5 as proxies of biological productivity in the Middle East during the Palaeocene and the latest Palaeocene benthic extinction event. Terra Nova, 9, 95–99. doi: 10.1111/j.1365-3121.1997.tb00011.x

Schneider, R.R., Price, B., Müller, P.J., Kroon, D., Alexander, I., 1997. Monsoon related variations in Zaire (Congo) sediment load and influence of fluvial silicate supply to productivity in the east equatorial Atlantic during the last 200,000 years. Paleoceanography, 12, 463–481. Click to copy the URI to your clipboard.https://doi.org/10.1029/96PA03640

Schnetger, B., 1992. Chemical composition of loess from a local and wordwide view. Neues Jahrbuch Mineralogische Abhandlungen, Monatshefte H. 1, pp. 29–47.

Schnetger, B., Brumsack, H.-J., Schale, H., Hinrichs, J., Dittert, L., 2000. Geochemical characteristics of deep-sea sediments from the Arabian Sea: a high-resolution study. Deep Sea Research Part II: Topical Studies in Oceanography, 47, 2735–2768. https://doi.org/10.1016/S0967-0645(00)00047-3

Schouten, S., van Kaam-Peters, H.M.E., Rijpstra, W.I.C., Schoell, M., Sinnighe Damste, J.S., 2000. Effects of an oceanic anoxic event on the stable carbon isotopic composition of early Toarcian carbon. American Journal of Science, 300, 1–22. https://doi.org/10.2475/ajs.300.1.1

Schwark, L., Frimmel, A., 2004. Chemostratigraphy of the Posidonia Black Shale, SW-Germany II. Assessment of extent and persistence of photic-zone anoxia using aryl isoprenoid distributions. Chemical Geology, 206, 231–248. doi:10.1016/j.chemgeo.2003.12.008

Seilacher, A., 1967. Bathymetry of trace fossils. Marine Geology, 5, 413–428. https://doi.org/10.1016/0025-3227(67)90051-5

Silva, R.L., Duarte, L.V., Wach, G.D., Ruhl, M., Sadki, D., Gómez, J.J., Hesselbo, S.P., Xu, W., O'Connor, D., Rodrigues, B., Mendonça Filho, J.G., 2021a. An Early Jurassic (Sinemurian–Toarcian) stratigraphic framework for the occurrence of Organic Matter Preservation Intervals (OMPIs). Earth-Science Reviews, 221, 103780.

Silva, R., Ruhl, M., Barry, C., Reolid, M., Ruebsam, W., 2021b. Pacing of late Pliensbachian and early Toarcian carbon cycle perturbations and environmental change in the westernmost Tethys (La Cerradura Section, Subbetic zone of the Betic Cordillera, Spain). In M. Reolid, L.V. Duarte, E. Mattioli, W. Ruebsam (Eds.), Carbon Cycle and Ecosystem Response to the Jenkyns Event in the Early Toarcian (Jurassic) (Vol. 514, pp. 387–408). Geological Society, London, UK: Geological Society Special Publications.

Sinnighe-Damste, J.S., Kuypers, M.M.M., Schoutem S., Schulte, S., Rullkötter, J., 2003. The lycopane/C 31 n-alkane ratio as a proxy to assess palaeoxicity during sediment deposition. Earth and Planetary Science Letters, 209, 215–226. doi: 10.1016/S0012-821X(03)00066-9

Storm, M.S., Hesselbo, S.P., Jenkyns, H.C., Ruhl, M., Ullmann, C.V., Xu, W., Leng, M.J., Riding, J.B., Gorbanenko, O., 2020. Orbital pacing and secular evolution of the Early Jurassic carbon cycle. Proceedings of the National Academy of Sciences, 117, 3974–3982. https://doi.org/10.1073/pnas.1912094117

Suan, G., Mattioli, E., Pittet, B., Mailliot, S., Lécuyer, C., 2008. Evidence for major environmental perturbation prior to and during the Toarcian (Early Jurassic) oceanic anoxic event from the Lusitanian Basin, Portugal. Paleocenography, 23, PA1202, doi:10.1029/2007PA001459

Suan, G., Rulleau, L., Mattioli, E., Suchéeras-Marx, B., Rousselle, B., Pittet, B., Vincent, P., Martin, J.E., Léna, A., Spangenberg, J.E., Fölllmi, K.B., 2013. Palaeoenvironmental significance of Toarcian black shales and event deposits from southern Beaujolais, France. Geological Magazine, 150, 728–742. https://doi.org/10.1017/S0016756812000970

Suan, G., van de Schootbrugge, B., Adatte, T., Fiebig, J., Oschmann, W., 2015. Calibrating the magnitude of the Toarcian carbon cycle perturbation. Paleoceanography, 30, 495–509. doi:10.1002/2014PA002758

Suan, G., Schlögl, J., Mattioli, E., 2016. Bio- and chemostratigraphy of the Toarcian organic-rich deposits of some key successions of the Alpine Tethys. Newsletters on Stratigraphy, 49/3, 401–419. doi: 10.1127/nos/2016/0078

Suan, G., Schöllhorn, I., Schlögl, J., Segit, T., Mattioli, E., Lécuyer, C., Fourel, F., 2018. Euxinic conditions and high sulfur burial near the European shelf margin (Pieniny Klippen Belt, Slovakia) during the Toarcian oceanic anoxic event. Global and Planetary Change, 170, 246–259. https://doi.org/10.1016/j.gloplacha.2018.09.003

Svensen, H.H., Planke, S., Chevallier, L., Malthe-Sørenssen, A., Corfu, F., Jamtveit, B., 2007. Hydrothermal venting of greenhouse gases triggering Early Jurassic global warming. Earth and Planetary Science Letters, 256, 554–566. doi:10.1016/j.epsl.2007.02.013

Sweere, T., van den Boorn, S., Dickson, A.J., Reichart, G.-J., 2016. Definition of new trace-metal proxies for the controls on organic matter enrichment in marine sediments based on Mn, Co, Mo and Cd concentrations. Chemical Geology, 441, 235–245. http://dx.doi.org/10.1016/j.chemgeo.2016.08.028

Them, T.R., Gill, B.C., Selby, D., Gröcke, D.R., Friedman, R.M., Owens, J.D., 2017. Evidence for rapid weathering response to climatic warming during the Toarcian Oceanic Anoxic Event. Scientific Reports, 7, 5003, doi: 10.1038/s41598-017-05307-y

Thibault, N., Ruhl, M., Ullmann, V., Korte, C., Kemp, D.B., Gröcke, D.R., Hesselbo, S.P., 2018. Proceedings of the Geologists' Association, 129, 372–391. https://doi.org/10.1016/j.pgeola.2017.10.007

Tintori, A., 1977. Toarcian fishes from the Lombardy Basin. Bollettino della Società Paleontologica Italiana, 16, 143–152.

Trabucho-Alexandre, J., Dirkx, R., Veld, H., Klaver, G., De Boer, P., 2012. Toarcian black shales in the Dutch Central Graben: record of energetic, variable depositional conditions during an oceanic anoxic event. Journal of Sedimentary Research, 82, 104–120. https://doi.org/10.2110/jsr.2012.5

Trecalli, A., Spangenberg, J., Adatte, T., Föllmi, K.B., Parente, M., 2012. Carbonate platform evidence of ocean acidification at the onset of the early Toarcian oceanic anoxic event. Earth and Planetary Science Letters, 357–358, 214–225. https://doi.org/10.1016/j.epsl.2012.09.043

Tremolada, F., van de Schootbrugge, B., Erba, E., 2005. Early Jurassic schizosphaerellid crisis in Cantabria, Spain: Implications for calcification rates and phytoplankton evolution across the Toarcian oceanic anoxic event. Paleoceanography, 20, PA2011, doi: 10.1029/2004PA001120

Tribovillard, N., Algeo, T.J., Lyons, T., Riboulleau, A., 2006. Trace metals as paleoredox and paleoproductivity proxies: an update. Chemical Geology, 232, 12–32. https://doi.org/10.1016/j.chemgeo.2006.02.012

Turgeon, S., Brumsack, H.-J., 2006. Anoxic vs dysoxic events reflected in sediment geochemistry during the Cenomanian–Turonian Boundary Event (Cretaceous) in the Umbria–Marche Basin of central Italy. Chemical Geology, 234, 321–339. https://doi.org/10.1016/j.chemgeo.2006.05.008

Tyson, R.V., Pearson, T.H., 1991. Modern and ancient continental shelf anoxia: an overview. In: R.V. Tyson, T.H. Pearson (Eds.), Modern and Ancient Continental Shelf Anoxia (Vol. 58, pp. 1–24). London, UK: Geological Society Special Publication.Geological Society of London Special Publication. https://doi.org/10.1144/GSL.SP.1991.058.01.01

Wedepohl, K.H., 1971. Environmental influences on the chemical composition of shales and clays. In L.H. Ahrens, F. Press, S.K. Runcorn, H.C. Urey (Eds.), Physics and Chemistry of the Earth (Vol. 8, pp. 305–333). Oxford, UK: Pergamon.

Ullmann, C.V., Hesselbo, S.P., Korte, C., 2013. Tectonic forcing of Early to Middle Jurassic seawater Sr/Ca. Geology, 41, 211–1214. https://doi.org/10.1130/G34817.1

van Breugel, Y., Baas, M., Schouten, S., Mattioli, E., Damsté, J.S.S., 2006. Isorenieratane record in black shales from the Paris Basin, France: Constraints on recycling of respired CO2 as a mechanism for negative carbon isotope shifts during the Toarcian oceanic anoxic event. Paleoceanography, 21, PA4220, https://doi.org/10.1029/2006PA001305.

van de Schootbrugge, B., Richoz, S., Pross, J., Luppold, F.W., Hunze, S., Wonik, T., Blau, J., Meister, C., van der Weijst, C.M.H., Suan, G., Fraguas, A., Fiebig, J., Herrle, J.O., Guex, J., Little, C.T.S., Wignall, P.B., Püttmann, W., Oschmann, W., 2019. The Schandelah Scientific Drilling Project: A 25-million year record of Early Jurassic palaeoenvironmental change from northern Germany. Newsletters on Stratigraphy, 52/3, 249–296. doi: 10.1127/nos/2018/0259

Vetö, I., Demény, A., Hertelendi, E., Heteéyi, M., 1997. Estimation of primary productivity in the Toarcian Tethys – A novel approach based on TOC, reduced sulphur and manganese contents. Palaeogeography, Palaeoclimatology, Palaeoecology, 132, 355–371. https://doi.org/10.1016/S0031-0182(97)00053-9

Vetö, I., Demény, A., Hertelendi, E., Hetényi, M., 1997. Estimation of primary productivity in the Toarcian Tethys—A novel approach based on TOC, reduced sulphur and manganese contents. Palaeogeography, Palaeoclimatology, Palaeoecology, 132, 355–371.

Visentin, S., Erba, E., 2021. High resolution calcareous nannofossil biostratigraphy across the Toarcian Oceanic Anoxic Event in Northern Italy: clues from the Sogno and Gajum Cores (Lombardy Basin, Southern Alps). Rivista Italiana di Paleontologia e Stratigrafia (Research in Paleontology and Stratiraphy), 127, 539–556.

Visentin, S., Erba, E., Mutterlose, J., 2021. Bio- and chemostratigraphy of the Posidonia Shale: a new database for the Toarcian Oceanic Anoxic Event from northern Germany. Newsletters on Stratigraphy, 55/2, 173–198. doi: 10.1127/nos/2021/0658

Wang, X., Lang, L., Hua, T., Zhang, C., Li, H., 2017. The effects of sorting by Aeolian processes on the geochemical characteristics of surface materials: a wind tunnel experiment. Frontiers of Earth Science, 12, 86–94. https://doi.org/10.1007/s11707-017-0619-2

Wang, Y., Ossa, F.O., Wille, M., Schurr, S., Saussele, M.-E., Scmid-Röhl, Schoenberg, R., 2020. Evidence for local carbon-cycle perturbations superimposed on the Toarcian carbon isotope excursion. Geobiology, 18, 682–709. doi: 10.1111/gbi.12410

Wedepohl, K.H., 1971. Environmental influences on the chemical composition of shales and clays. In L.H. Ahrens, F. Press, S.K. Runcorn, H.C. Urey (Eds.), Physics and Chemistry of the Earth (Vol. 8, pp. 305–333). Oxford, UK: Pergamon.

Wedepohl, K.H., 1991. The composition of the upper earth's crust and the natural cycles of selected metals. Metals in natural raw materials. Natural resources. In: E. Merian (Ed.), Metals and their Compounds in the Environment (pp. 3 – 17). Weinheim: VCH.

Winterer, E.L., Bosellini, A., 1981. Subsidence and sedimentation on Jurassic passive continental margin, Southern Alps, Italy. AAPG bulletin, 65, 394-421. https://doi.org/10.1306/2F9197E2-16CE-11D7-8645000102C1865D

Woodfine, R.G., Jenkyns, H.C., Sarti, M., Baroncini, F., Violante, C., 2008. The response of two Tethyan carbonate platforms to the early Toarcian (Jurassic) oceanic anoxic event: environmental change and differential subsidence. Sedimentology, 55, 1011–1028. https://doi.org/10.1111/j.1365-3091.2007.00934.x

Xu, W., Ruhl, M., Jenkyns, H.C., Hesselbo, S.P., Riding, J.B., Selby, D., Naafs, B.D.A., Weijers, J.W., Pancost, R.D., Tegelaar, E.W. and Idiz, E.F., 2017. Carbon sequestration in an expanded lake system during the Toarcian oceanic anoxic event. Nature Geoscience, 10, 129–134.

Xu, W., Ruhl, M., Jenkyns, H.C., Leng, M.J., Huggett, J.M., Minisini, D., Ullmann, C.V., Riding, J.B., Weijers, J.W., Storm, M.S., Percival, L.M., 2018. Evolution of the Toarcian (Early Jurassic) carbon-cycle and global climatic controls on local sedimentary processes (Cardigan Bay Basin, UK). Earth and Planetary Science Letters, 484, 396–411. https://doi.org/10.1016/j.epsl.2017.12.037

FIGURE CAPTIONS

Figure 1 – A. Palaeogeographic position of the study area during the Toarcian (~180 Ma) (modified after Ruhl et al., 2016). B. Paleogeographic map of the Northwestern Tethys during the Toarcian (~180 Ma) (modified after Ruebsam et al., 2018). C. Schematic cross-section across the Lombardy Basin during the Toarcian (~180 Ma) (modified after Erba et al., 2022). D. Nannofossil biostratigraphy (Visentin and Erba, 2021), lithostratigraphy (Erba et al., 2019b) and chemostratigraphy (Erba et al., 2022) of the Sogno Core (modified after Erba et al., 2022). Carbon isotopes on bulk carbonate ($\delta^{13}C_{carb}$) and bulk organic matter ($\delta^{13}C_{org}$) show samples below (red dots), within (white, grey and black dots; lithological units 7, 6, and 5 of Erba et al., 2019b, 2022) and above the "Fish Level" (blue dots). The lower and the upper part of the Jenkyns Event, J1 (light yellow box) and J2 (dark yellow box), are indicated as defined in Erba et al. (2022).

Figure 2 – Average enrichment factors (EFs) for samples coming from below, within (lithological units 7, 6, and 5 *sensu* Erba et al., 2019b, 2022) and above the Fish Level. Values for the discrete black shales BS1 and BS2 above the Fish Level are reported separately. EFs were calculated using average shale (AS) values from Wedepohl (1971, 1991), while EFs with an asterisk were estimated using local background concentrations reported in Table S1 in Supplementary material.

Figure 3 – Panel reporting organic and sedimentological data from the Fish Level interval in the Sogno Core. From left to right: nannofossil biostratigraphy (Visentin and Erba, 2021); schematic lithostratigraphy (Erba et al., 2019b); total organic carbon (TOC) and TOC/Al ratio; hydrogen index (HI); distribution of selected biomarkers ratios used to reconstruct organic matter type and redox conditions, i.e. carbon preference index (CPI), average chain length (ACL), and pristane/phytane (Pr/Ph) ratios as defined in Peters et al. (2005); pyrite distribution and

bioturbation amount in percentage; inferred organic matter preservation conditions. CPI, ACL, and Pr/Ph organic matter type and redox thresholds follow Peters et al. (2005). Different colours mark samples coming from the interval below, within (lithological units 7, 6, and 5 *sensu* Erba et al., 2019b, 2022) and above the Fish Level. Values for the discrete black shales BS1 and BS2 above the Fish Level are reported separately. Grey background shadings highlight lithological units 7, 6, and 5, while pale yellow and yellow shadings indicate J1 and J2 isotopic segments, respectively.

Figure 4 – Hydrogen Index (HI) *versus* Tmax diagram (modified van Krevelen diagram), showing kerogen type and thermal maturity of samples from the interval within (lithological units 7, 6, and 5 (*sensu* Erba et al., 2019b, 2022) and above the Fish Level. Values for the discrete black shales BS1 and BS2 above the Fish Level are reported separately. Samples with TOC ≤ 0.5 % are marked with a X.

Figure 5 – Ternary diagram of relative proportions of Al_2O_3 (×5), SiO_2, and CaO for samples from the Sogno Core. Different colours mark samples coming from the interval below, within (lithological units 7, 6, and 5 *sensu* Erba et al., 2019b, 2022) and above the Fish Level. Values for the discrete black shales BS1 and BS2 above the Fish Level are reported separately. For Al_2O_3 an arbitrary multiplier of 5 is used in order to improve distribution of the data points in the graph. The average shale (AS) composition (Wedepohl, 1971, 1991) and the carbonate dilution line (red line) are reported. See text for details.

Figure 6 – Cross-plots of lithogenic conservative elements (SiO_2, TiO_2, K_2O, Fe_2O_3, Rb, Zr) *versus* Al_2O_3 for samples from the Sogno Core. Different colours mark samples coming from the interval below, within (lithological units 7, 6, and 5 *sensu* Erba et al., 2019b, 2022) and above the Fish Level. Values for the discrete black shales BS1 and BS2 above Fish Level are reported

separately. The average shale (AS) line (following values in Wedepohl (1971, 1991)), which connects the origin of the graph to the average shale composition, is reported in each plot.

Figure 7 – Panel reporting elemental detrital and productivity proxies for the Sogno Core. From left to right: nannofossil biostratigraphy (Visentin and Erba, 2021); schematic lithostratigraphy (Erba et al., 2019b); $\delta^{13}C_{carb}$ and $\delta^{13}C_{org}$ chemostratigraphy (Erba et al., 2022); detrital (Zr_{xs}, Ti/Al, K/Al, K/Rb); productivity (Si_{xs}) element stratigraphic distribution. The vertical lines in the Ti/Al and K/Al graphs represent average shale (AS) compositions according to Wedepohl (1971, 1991). For the sake of readability, the Zr_{xs} and Si_{xs} axes are cropped. Element/Al background concentrations used to estimate excess values are reported in Table 1. Different colours mark samples coming from the interval below, within (lithological units 7, 6, and 5 *sensu* Erba et al., 2019b, 2022) and above the Fish Level. Values for the discrete black shales BS1 and BS2 above the Fish Level are reported separately. Grey background shadings highlight lithological units 7, 6, and 5, while pale yellow and yellow shadings indicate J1 and J2 isotopic segments of the Jenkyns Event, respectively. The position of the T-OAE is indicated by a white bar.

Figure 8 – Panel reporting elemental redox-sensitive proxies for the Sogno Core. From left to right: nannofossil biostratigraphy (Visentin and Erba, 2021); schematic lithostratigraphy (Erba et al., 2019b); $\delta^{13}C_{carb}$ and $\delta^{13}C_{org}$ chemostratigraphy (Erba et al., 2022); redox-sensitive (Mn_{xs}, As/Al, Mo/Al, V/Al, Cu/Al, Co/Al) element stratigraphic distribution. The vertical line in the As/Al, Mo/Al, V/Al, Cu/Al, and Co/Al graphs represents average shale (AS) composition according to Wedepohl (1971, 1991). For the sake of readability, the As/Al, Mo/Al, V/Al, Cu/Al, and Co/Al axes are cropped and the Mn_{xs} axis is in logarithmic scale. Element/Al background concentrations used to estimate excess values are reported in Table 1. Different colours mark

samples coming from the interval below, within (lithological units 7, 6, and 5 *sensu* Erba et al., 2019b, 2022) and above the Fish Level. Values for the discrete black shales BS1 and BS2 above the Fish Level are reported separately. Grey background shadings highlight lithological units 7, 6, and 5, while pale yellow and yellow shadings indicate J1 and J2 isotopic segments of the Jenkyns Event, respectively. The position of the T-OAE is indicated by a white bar.

Figure 9 – Cross-plot of Co_{EF} × Mn_{EF} *versus* Al (Sweere et al., 2016) for samples within the Fish Level (lithological units 7, 6, and 5 *sensu* Erba et al., 2019b, 2022) and the two discrete black shales BS1 and BS2 in the interval above the Fish Level. See text for details.

Figure 10 – Scheme reporting the stratigraphic variation of the various processes as recorded in the Sogno Core. Schematic lithostratigraphy and chemostratigraphy after Erba et al., (2019, 2022).

Figure 11a – Schematic depositional model (not to scale) representing the major chemical processes involved during the deposition of the studied record during the T-OAE. The division of the various intervals is reported in Figure 10. In particular: A. Interval deposited during the earliest phases of the T-OAE before deposition of the Fish Level; B. Interval right below the Fish Level; C. Lithological unit 7 of the Fish Level; D. Lithological unit 6 of the Fish Level. See text for details.

Figure 11b – Schematic depositional model (not to scale) representing the major chemical processes involved during the deposition of the studied record during the T-OAE. The division of the various intervals is reported in Figure 10. In particular: E. Lithological unit 5 of the Fish Level; F. Interval right above the Fish Level; G. Interval deposited during the uppermost part of the J2 segment. H. Interval deposited during the latest phases of the T-OAE. See text for details.

Table 1 – Lithostratigraphy, average and maximum TOC, and palaeobathymetry of key-sections from the epicontinental northern Europe, marginal proto-Atlantic, and Alpine-Mediterranean Tethys used for correlation with the Sogno Core record.

Figure 12 – Detrital input, primary productivity and redox conditions reconstructed on the basis of elemental data, organic geochemistry and integrated with bioturbation data at Sogno Core (Italy), Dogna (Italy), Peniche (Portugal), Creux de l'Ours (Switzerland), Bächental (Austria), Réka Valley (Hungary), Sancerre (France), Rietheim (Switzerland), Dotternhausen (Germany), Shandelah (Germany), and Yorkshire (UK). Sogno Core: $\delta^{13}C_{carb}$ and $\delta^{13}C_{org}$ (Erba et al., 2022), black shales position (Erba et al., 2022), detrital input, primary productivity and redox conditions (this study), integrated with bioturbation data (this study) − no available data on photic-zone euxinia (PZE). Dogna: $\delta^{13}C_{carb}$ and $\delta^{13}C_{org}$ (Jenkyns et al., 2001; Dickson et al., 2017), redox conditions (Farrimond et al., 1994; Dickson et al., 2017) – lithological data are not provided for Dogna, preventing the identification of black shales. Peniche: $\delta^{13}C_{carb}$ and $\delta^{13}C_{org}$ (Hesselbo et al., 2007), black shales position (Hesselbo et al., 2007; Hermoso et al., 2009b), detrital input and productivity (Fantasia et al., 2019a), redox conditions (Hermoso et al., 2009b; Fantasia et al., 2019a), bioturbation (Suan et al., 2008) − no available data on PZE. Creux de l'Ours: $\delta^{13}C_{org}$ (Fantasia et al., 2018), dark grey marls position (Fantasia et al., 2018, 2019b), detrital input, productivity, and redox conditions (Fantasia et al., 2018). Bächental: $\delta^{13}C_{carb}$ and $\delta^{13}C_{org}$ (Neumeister et al., 2015), black shales stratigraphic position (Neumeister et al., 2015; Suan et al., 2016), redox conditions (Neumeister et al., 2015). Réka Valley: $\delta^{13}C_{org}$ (Müller et al., 2017), black shales stratigraphic position and redox conditions (Ruebsam et al., 2018). Sancerre: $\delta^{13}C_{carb}$ (Hermoso et al., 2009a, 2012) and $\delta^{13}C_{org}$ (Hermoso et al., 2012), black shales stratigraphic position (Hermoso et al., 2009a), detrital input (Hermoso et al., 2013), redox conditions (Hermoso

et al., 2009b, 2013), bioturbation (Hermoso et al., 2009a, 2013) – no available data on PZE. Rietheim: $\delta^{13}C_{carb}$ and $\delta^{13}C_{org}$ (Montero-Serrano et al., 2015), black shales stratigraphic position (Montero-Serrano et al., 2015; Fantasia et al., 2018), detrital input, productivity and redox conditions (Montero-Serrano et al., 2015), bioturbation (Montero-Serrano et al., 2015; Fantasia et al., 2018) – no available data on PZE. Dotternhausen: $\delta^{13}C_{carb}$ and $\delta^{13}C_{org}$ (Schouten et al., 2000; Röhl and Schmid-Röhl et al., 2005), black shales stratigraphic position (Schouten et al., 2000; Röhl and Schmid-Röhl et al., 2005; Dickson et al., 2017), redox conditions (Dickson et al., 2017; Baroni et al., 2018; Wang et al., 2020), bioturbation (Röhl et al., 2001; Schwark and Frimmel, 2004; Röhl and Schmid-Röhl et al., 2005), PZE (Schouten et al., 2000; Schwark and Frimmel, 2004). Schandelah: $\delta^{13}C_{org}$ (van Schootbrugge et al., 2019a; Visentin et al., 2021), black shales stratigraphic position (Visentin et al., 2021), redox conditions (Baroni et al., 2018) – no available data on PZE. Yorkshire: $\delta^{13}C_{org}$ (Cohen et al., 2004; Kemp et al., 2005), black shales stratigraphic position (Hesselbo et al., 2000; Cohen et al., 2004; Kemp et al., 2005; Dickson et al., 2017), detrital input (Thibault et al., 2018), primary productivity (Remirez and Algeo, 2020a), redox conditions (McArthur et al., 2008; Dickson et al., 2017; Baroni et al., 2018; Thibault et al., 2018; McArthur, 2019; Houben et al., 2021), bioturbation (Caswell and Frid, 2017), PZE (Bowden et al., 2006; French et al., 2014). See text for details.

Figure 13 –Palaeogeographic map of the epicontinental northern Europe and Tethyan areas to the south during the Toarcian (~180 Ma) (modified after Ruebsam et al., 2018). The palaeo-location of the Sogno Core is reported, together with those of other key sections discussed in the text and reported in Figure 12. Distribution of anoxia modified after Baroni et al. (2018) and Ruebsam et al. (2018). A pink shade indicates the distribution of Mn-rich carbonates in the Alpine-Mediterranean Tethys as described in Jenkyns et al. (1991).

1651

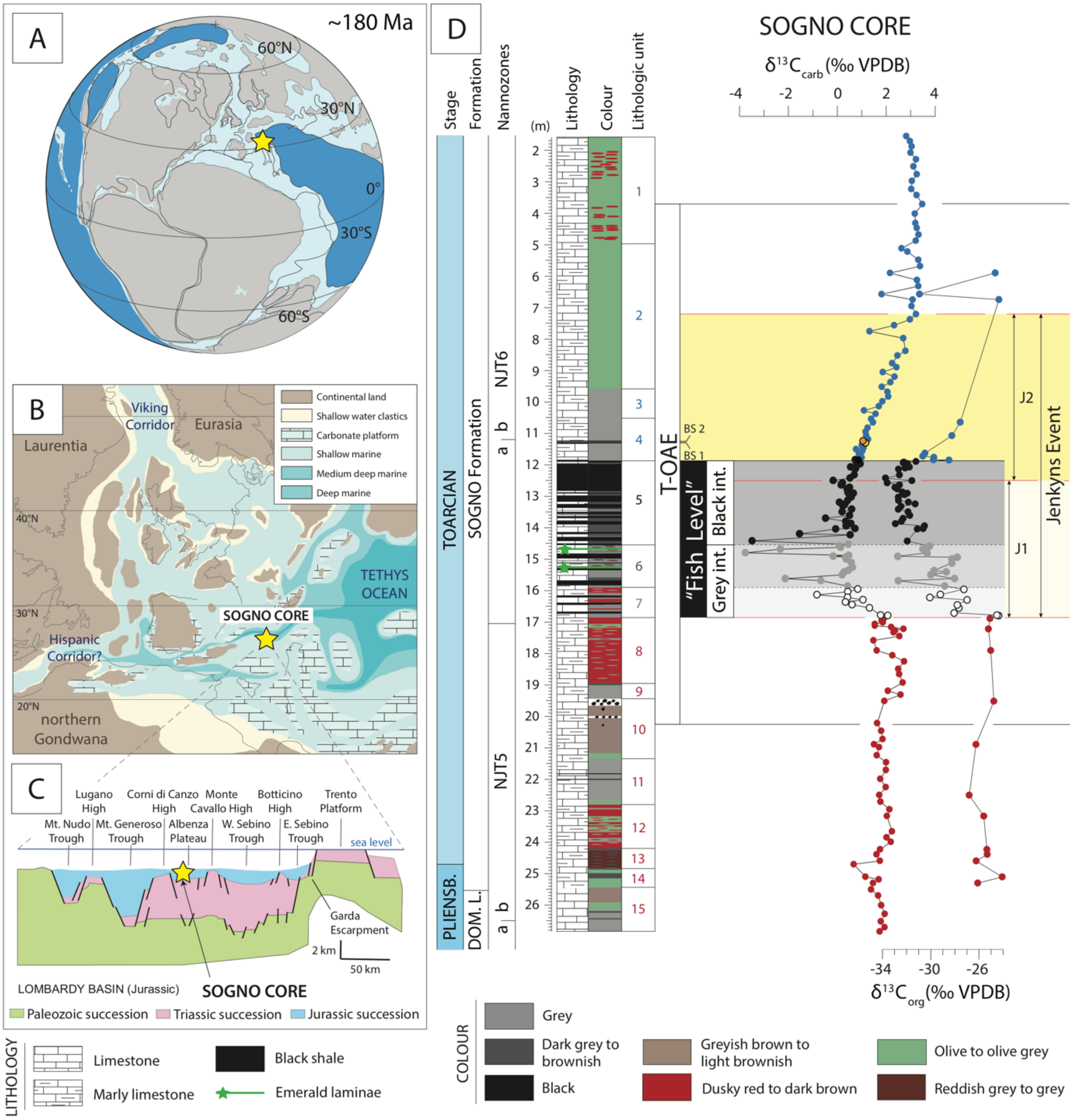
A
~180 Ma
60°N
30°N
0°
30°S
60°S
B
Viking Corridor
Eurasia
Laurentia
Continental land
Shallow water clastics
Carbonate platform
Shallow marine
Medium deep marine
Deep marine
40°N
30°N
20°N
TETHYS OCEAN
SOGNO CORE
Hispanic Corridor?
northern Gondwana
C
Lugano High
Corni di Canzo High
Monte Cavallo High
Botticino High
Trento Platform
Mt. Nudo Trough
Mt. Generoso Trough
Albenza Plateau
W. Sebino Trough
E. Sebino Trough
sea level
Garda Escarpment
2 km
50 km
LOMBARDY BASIN (Jurassic)
SOGNO CORE
Paleozoic succession
Triassic succession
Jurassic succession
D
Stage
Formation
Nannozones
(m)
Lithology
Colour
Lithologic unit
SOGNO CORE
δ13Ccarb (‰ VPDB)
-4
-2
0
2
4
TOARCIAN
PLIENSB.
SOGNO Formation
DOM. L.
NJT6
NJT5
a
b
T-OAE
"Fish Level"
Black int.
Grey int.
BS 2
BS 1
J1
J2
Jenkyns Event
-34
-30
-26
δ13Corg (‰ VPDB)
LITHOLOGY
Limestone
Marly limestone
Black shale
Emerald laminae
COLOUR
Grey
Dark grey to brownish
Black
Greyish brown to light brownish
Dusky red to dark brown
Olive to olive grey
Reddish grey to grey

Figure 1

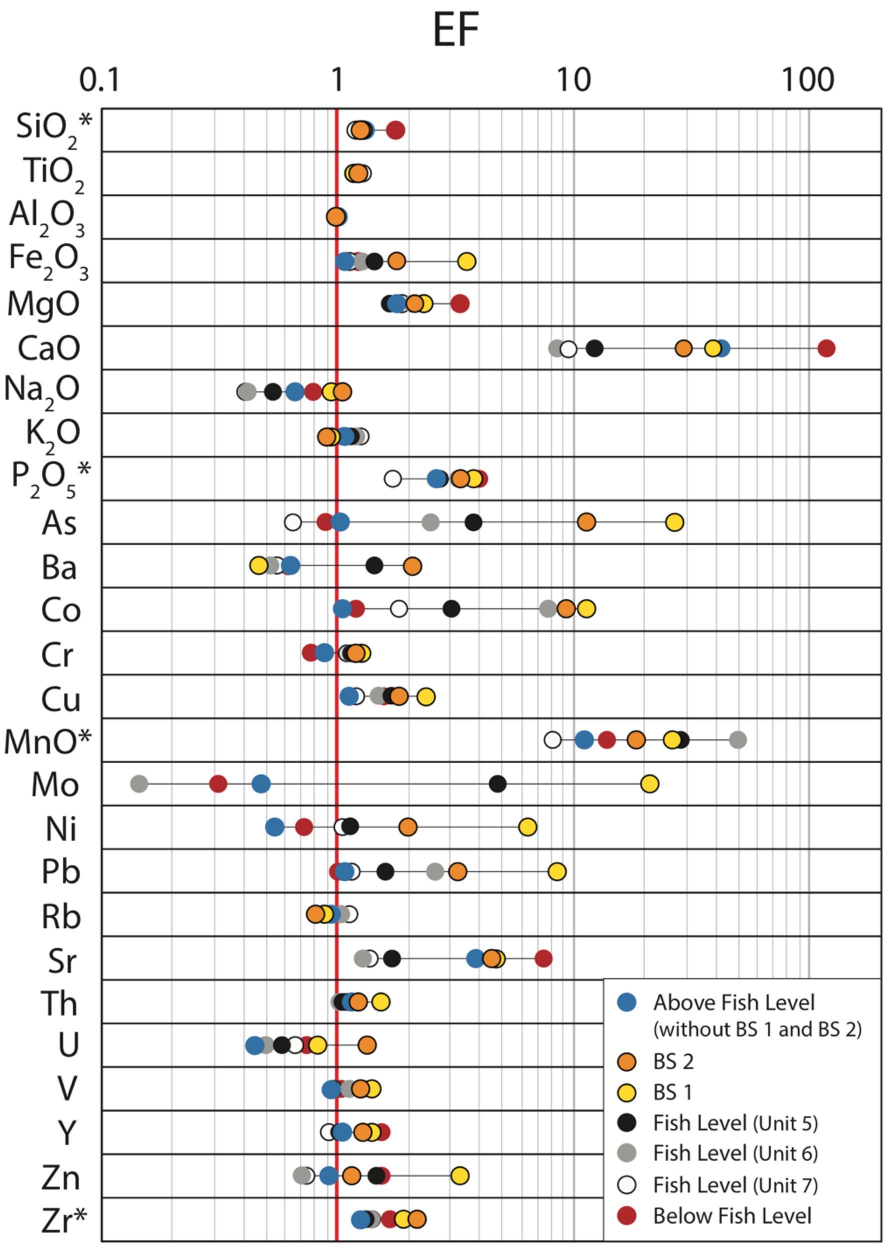

1654

1655 **Figure 2**

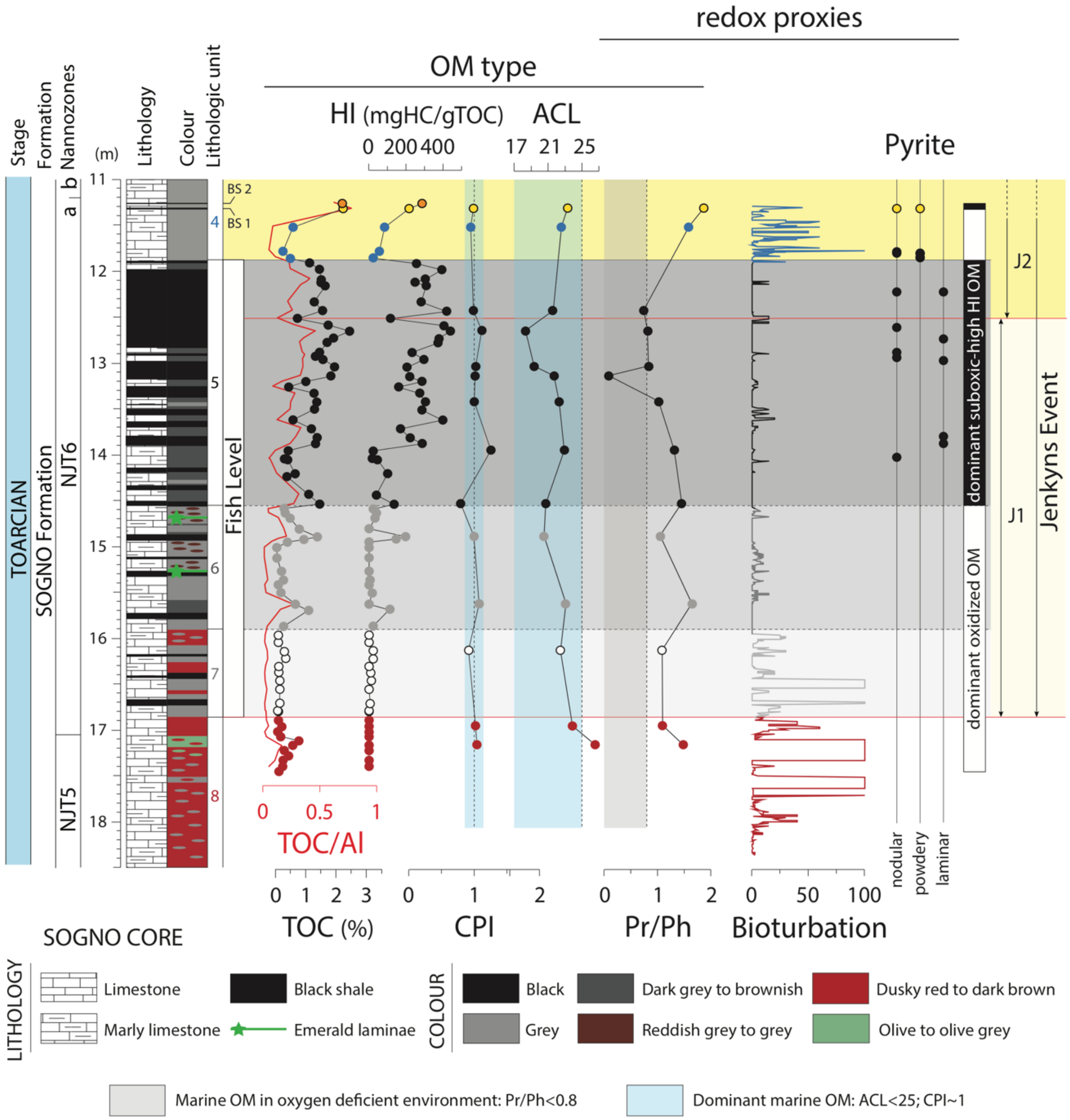
redox proxies
OM type
HI (mgHC/gTOC)
0 200 400
ACL
17 21 25
Pyrite
Stage
Formation
Nannozones
(m)
Lithology
Colour
Lithologic unit
a
b
11
12
13
14
15
16
17
18
BS 2
BS 1
4
5
6
7
8
TOARCIAN
SOGNO Formation
NJT6
NJT5
Fish Level
0
0.5
1
TOC/Al
0 1 2 3
TOC (%)
0 1 2
CPI
0 1 2
Pr/Ph
0 50 100
Bioturbation
nodular
powdery
laminar
dominant suboxic-high HI OM
dominant oxidized OM
J2
J1
Jenkyns Event
SOGNO CORE
LITHOLOGY
Limestone
Marly limestone
Black shale
Emerald laminae
COLOUR
Black
Grey
Dark grey to brownish
Reddish grey to grey
Dusky red to dark brown
Olive to olive grey
Marine OM in oxygen deficient environment: Pr/Ph<0.8
Dominant marine OM: ACL<25; CPI~1

Figure 3

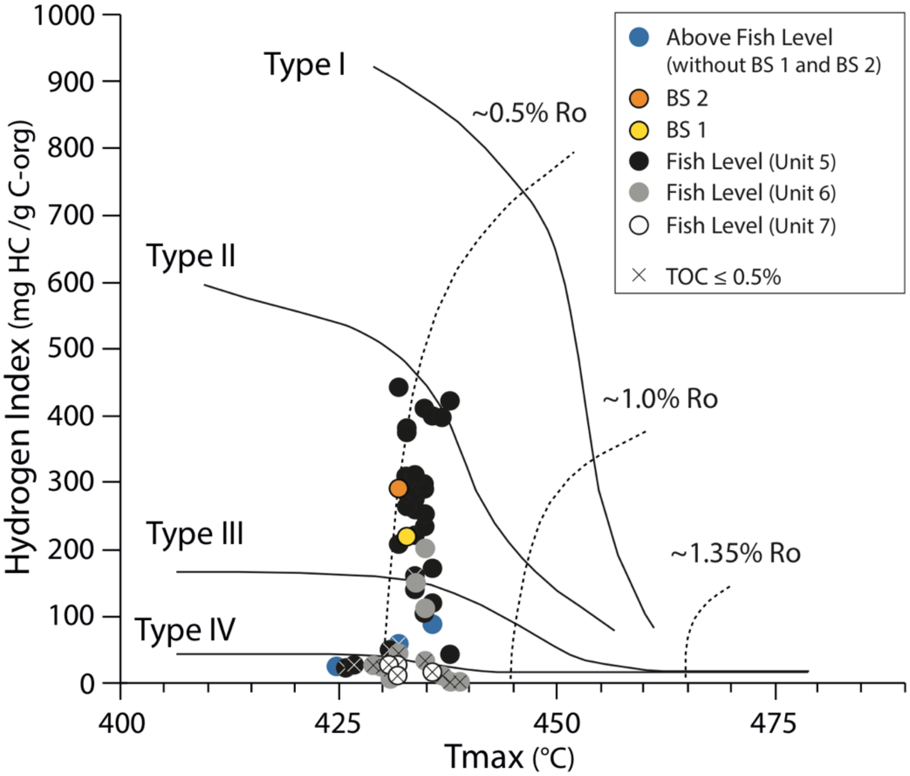

1000
900
800
700
600
500
400
300
200
100
0
Hydrogen Index (mg HC /g C-org)
400
425
450
475
Tmax (°C)
Type I
Type II
Type III
Type IV
~0.5% Ro
~1.0% Ro
~1.35% Ro
Above Fish Level (without BS 1 and BS 2)
BS 2
BS 1
Fish Level (Unit 5)
Fish Level (Unit 6)
Fish Level (Unit 7)
× TOC ≤ 0.5%

Figure 4

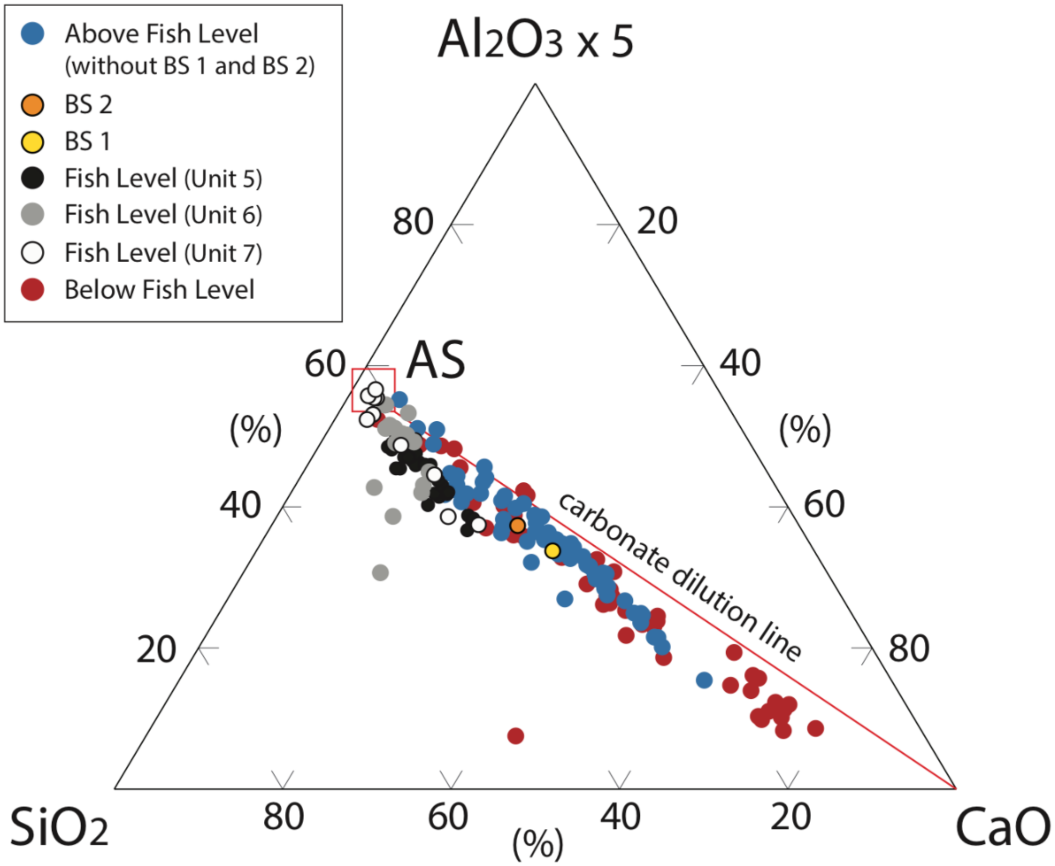

1661

1662 Figure 5

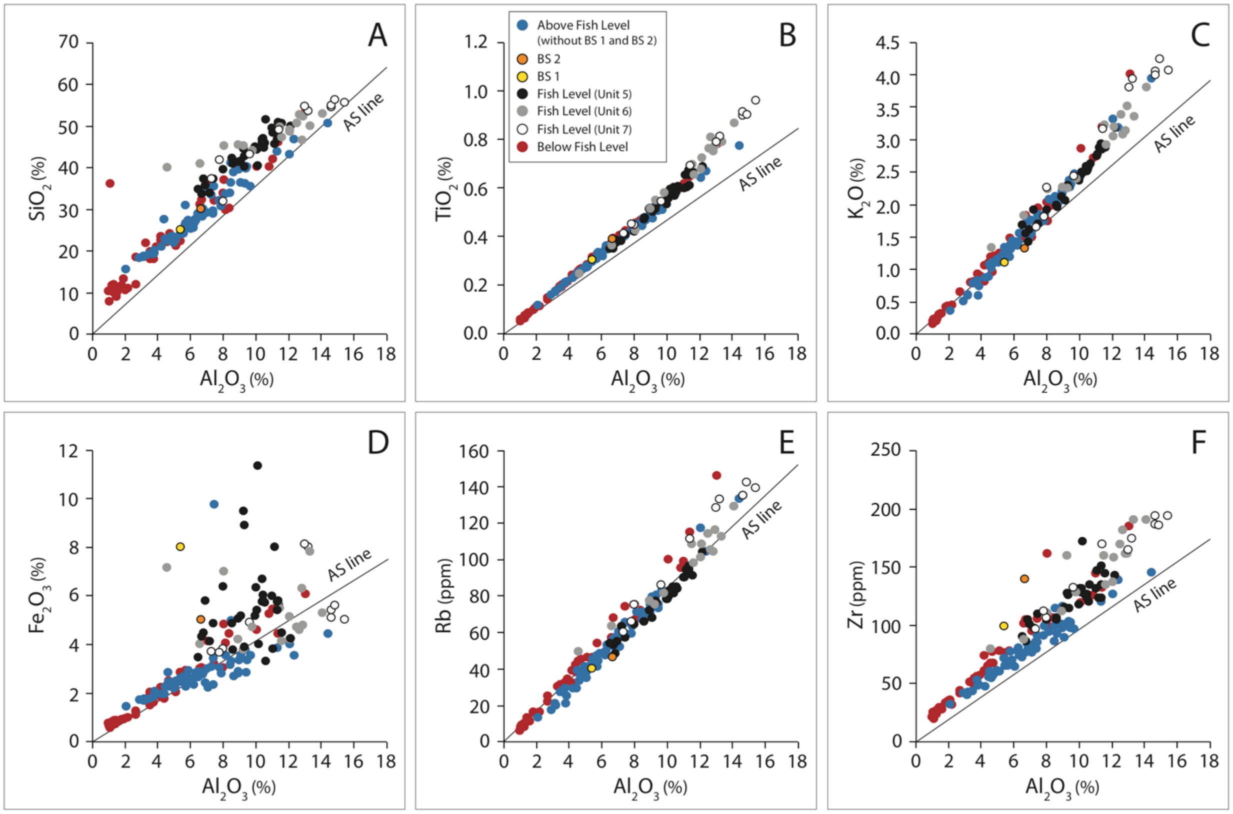
A
SiO$_2$ (%)
Al$_2$O$_3$ (%)
AS line
B
TiO$_2$ (%)
Al$_2$O$_3$ (%)
AS line
● Above Fish Level (without BS 1 and BS 2)
● BS 2
● BS 1
● Fish Level (Unit 5)
● Fish Level (Unit 6)
○ Fish Level (Unit 7)
● Below Fish Level
C
K$_2$O (%)
Al$_2$O$_3$ (%)
AS line
D
Fe$_2$O$_3$ (%)
Al$_2$O$_3$ (%)
AS line
E
Rb (ppm)
Al$_2$O$_3$ (%)
AS line
F
Zr (ppm)
Al$_2$O$_3$ (%)
AS line

Figure 6

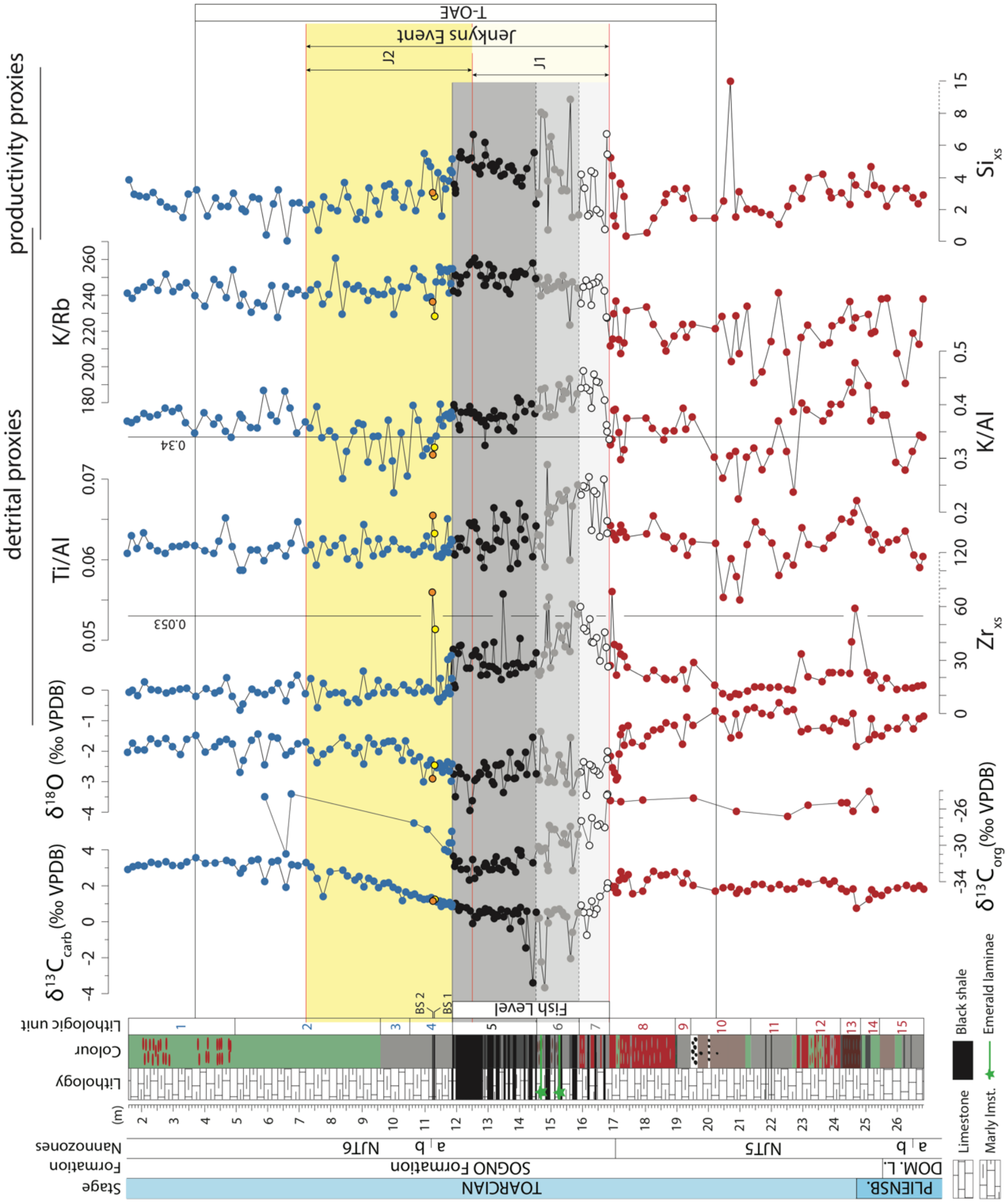
T-OAE
Jenkyns Event
J1
J2
productivity proxies
detrital proxies
Si$_{xs}$
0 2 4 6 8 10 15
K/Rb
180 200 220 240 260
K/Al
0.2 0.3 0.34 0.4 0.5
Ti/Al
0.05 0.053 0.06 0.07
Zr$_{xs}$
0 30 60 120
δ^{18}O (‰ VPDB)
-4 -3 -2 -1 0
δ^{13}C$_{org}$ (‰ VPDB)
-34 -30 -26
δ^{13}C$_{carb}$ (‰ VPDB)
-4 -2 0 2 4
Fish Level
BS 2
BS 1
Lithologic unit
1 2 3 4 5 6 7 8 9 10 11 12 13 14 15
Colour
Lithology
(m)
2 3 4 5 6 7 8 9 10 11 12 13 14 15 16 17 18 19 20 21 22 23 24 25 26
Nannozones
NJT6
a b
NJT5
Formation
SOGNO Formation
DOM. L.
Stage
TOARCIAN
PLIENSB.
Limestone
Marly lmst.
Black shale
Emerald laminae

Figure 7

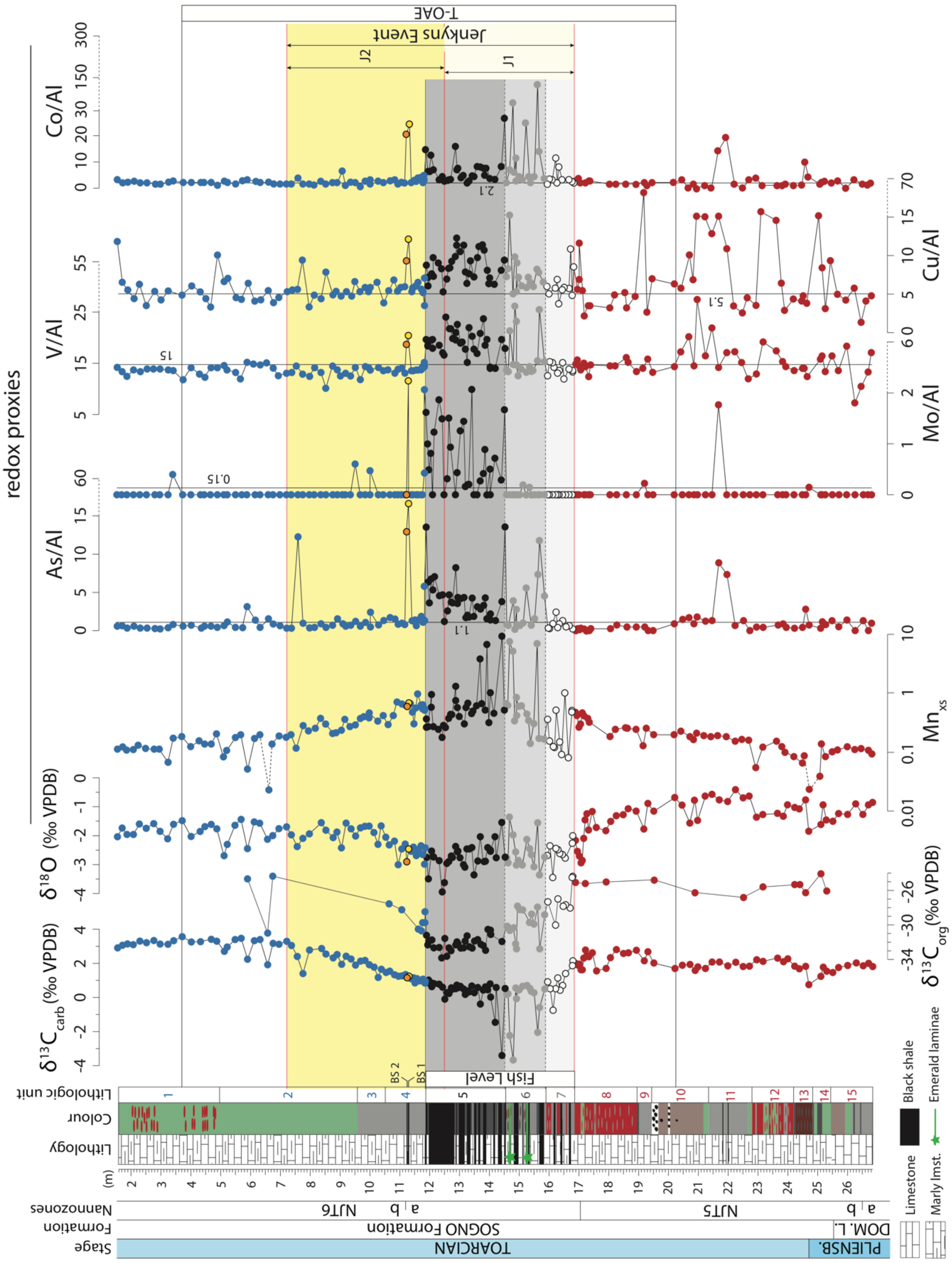
Stage
TOARCIAN
PLIENSB.
Formation
SOGNO Formation
DOM. L.
Nannozones
NJT6
NJT5
a
b
(m)
2
3
4
5
6
7
8
9
10
11
12
13
14
15
16
17
18
19
20
21
22
23
24
25
26
Lithology
Colour
Lithologic unit
1
2
3
4
5
6
7
8
9
10
11
12
13
14
15
BS 2
BS 1
Fish Level
δ13Ccarb (‰ VPDB)
δ18O (‰ VPDB)
δ13Corg (‰ VPDB)
Mnxs
As/Al
Mo/Al
V/Al
Cu/Al
Co/Al
redox proxies
T-OAE
Jenkyns Event
J1
J2
1.1
0.15
15
5.1
2.1
Limestone
Marly lmst.
Black shale
Emerald laminae

Figure 8

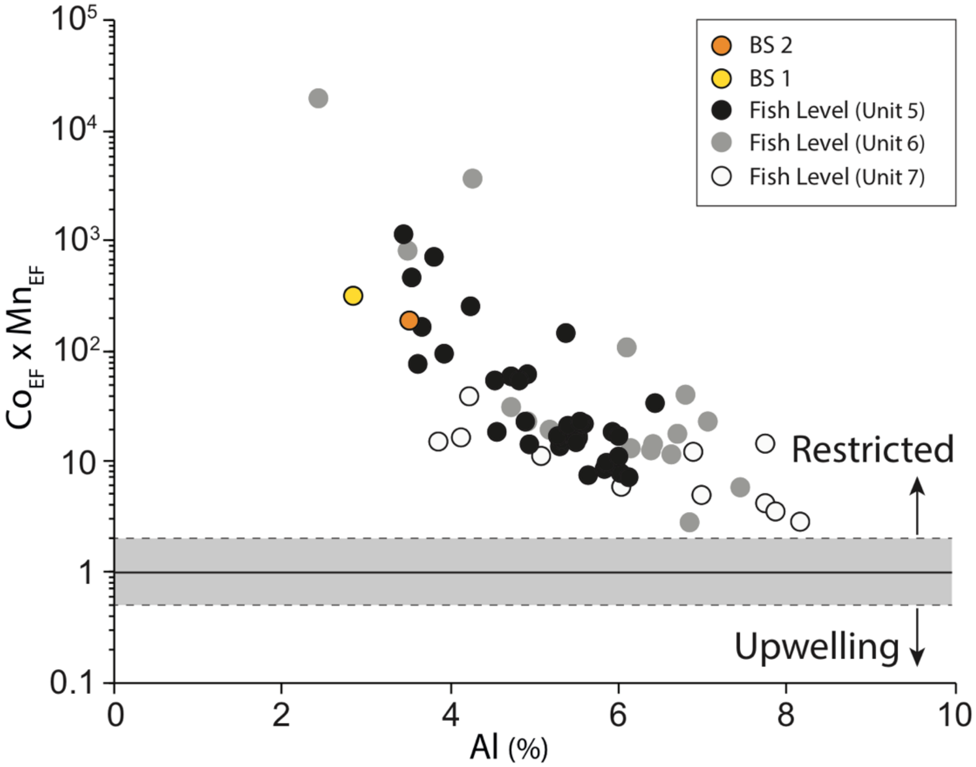

10⁵
10⁴
10³
10²
10
1
0.1
Co$_{EF}$ x Mn$_{EF}$
0
2
4
6
8
10
Al (%)
BS 2
BS 1
Fish Level (Unit 5)
Fish Level (Unit 6)
Fish Level (Unit 7)
Restricted
Upwelling

Figure 9

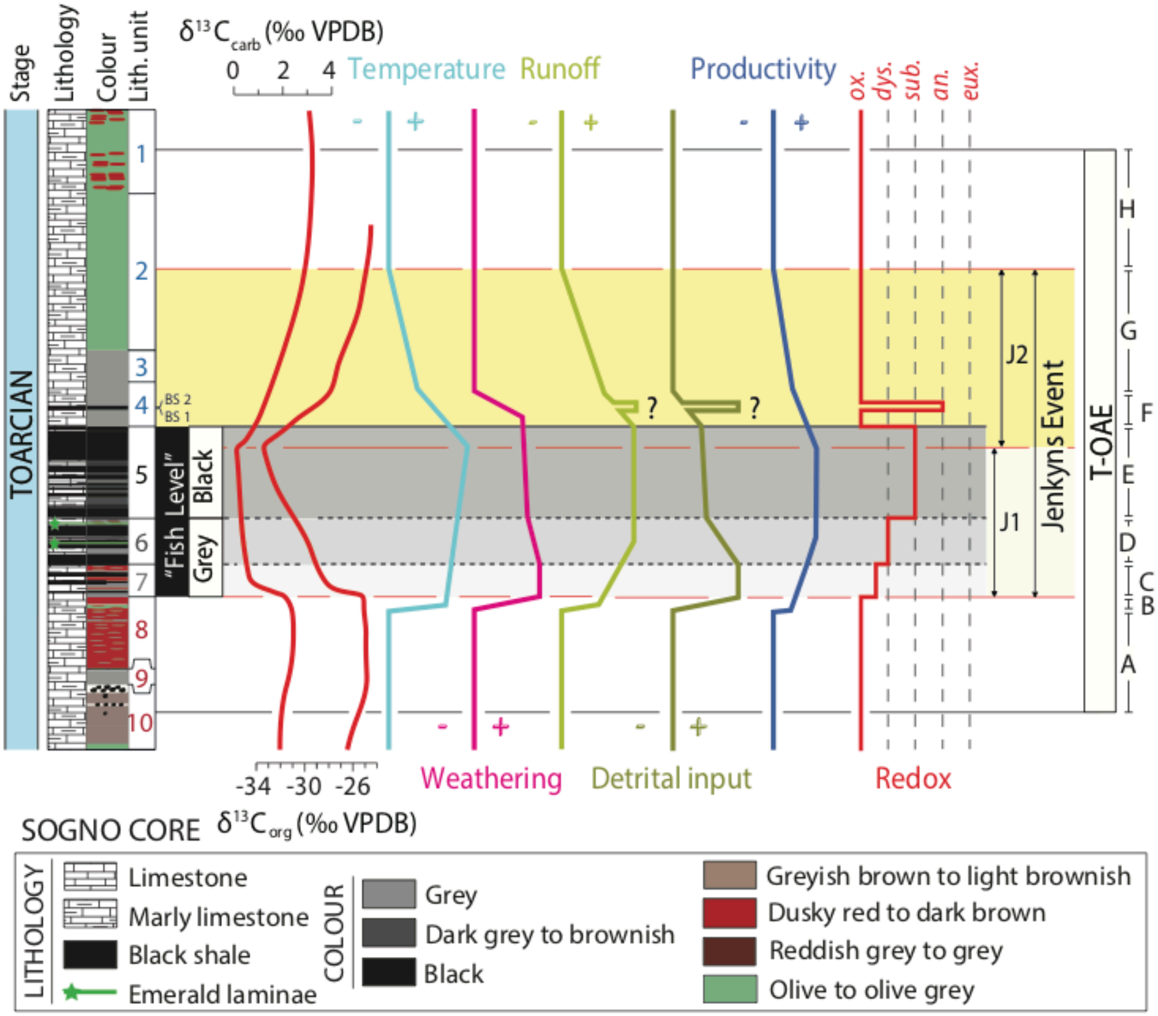
Stage
Lithology
Colour
Lith. unit
δ13Ccarb (‰ VPDB)
0 2 4
Temperature
Runoff
Productivity
ox.
dys.
sub.
an.
eux.
- +
TOARCIAN
1
2
3
4
BS 2
BS 1
5
6
7
8
9
10
"Fish Level"
Black
Grey
?
?
H
G
F
E
D
C
B
A
J2
J1
Jenkyns Event
T-OAE
-34 -30 -26
Weathering
Detrital input
Redox
SOGNO CORE
δ13Corg (‰ VPDB)
LITHOLOGY
Limestone
Marly limestone
Black shale
Emerald laminae
COLOUR
Grey
Dark grey to brownish
Black
Greyish brown to light brownish
Dusky red to dark brown
Reddish grey to grey
Olive to olive grey

Figure 10

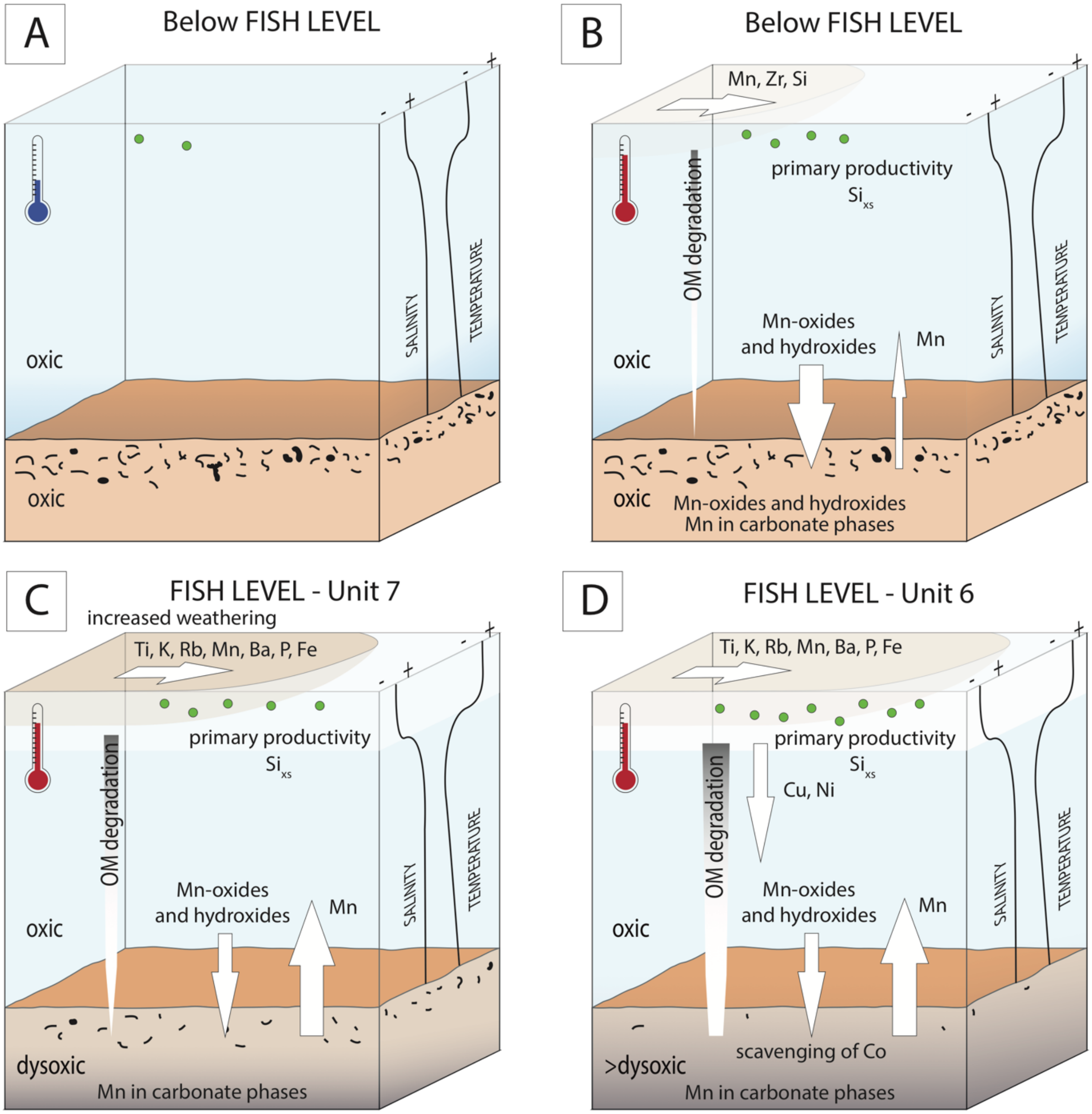
A
Below FISH LEVEL
oxic
oxic
SALINITY
TEMPERATURE
B
Below FISH LEVEL
Mn, Zr, Si
primary productivity
Si_{xs}
OM degradation
Mn-oxides
and hydroxides
Mn
oxic
oxic
Mn-oxides and hydroxides
Mn in carbonate phases
SALINITY
TEMPERATURE
C
FISH LEVEL - Unit 7
increased weathering
Ti, K, Rb, Mn, Ba, P, Fe
primary productivity
Si_{xs}
OM degradation
Mn-oxides
and hydroxides
Mn
oxic
dysoxic
Mn in carbonate phases
SALINITY
TEMPERATURE
D
FISH LEVEL - Unit 6
Ti, K, Rb, Mn, Ba, P, Fe
primary productivity
Si_{xs}
Cu, Ni
OM degradation
Mn-oxides
and hydroxides
Mn
oxic
>dysoxic
scavenging of Co
Mn in carbonate phases
SALINITY
TEMPERATURE
- +
- +

Figure 11a

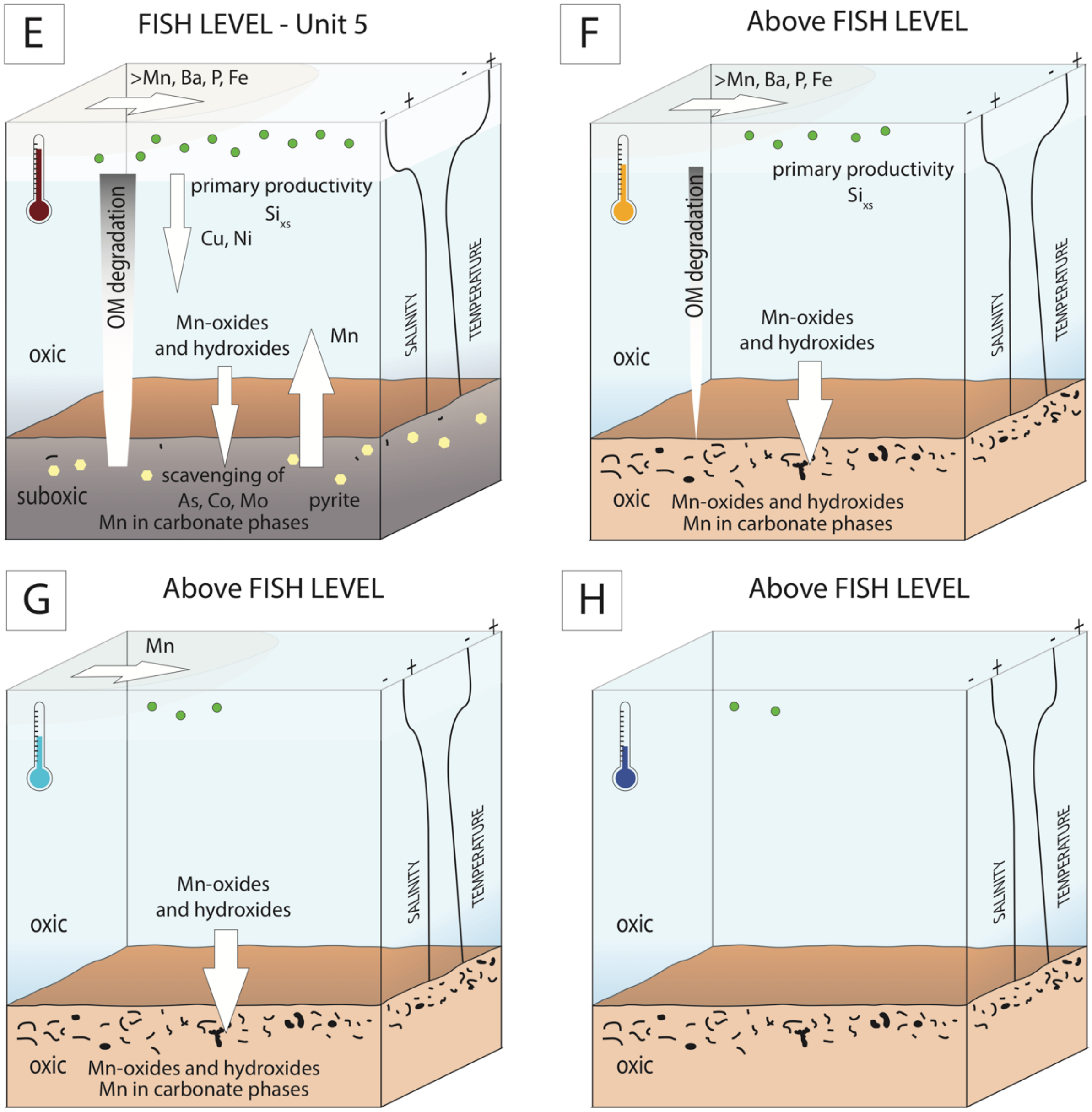
E
FISH LEVEL - Unit 5
>Mn, Ba, P, Fe
OM degradation
primary productivity
Si_{xs}
Cu, Ni
Mn-oxides
and hydroxides
Mn
oxic
suboxic
scavenging of
As, Co, Mo
pyrite
Mn in carbonate phases
SALINITY
TEMPERATURE
-
+
-
+
F
Above FISH LEVEL
>Mn, Ba, P, Fe
OM degradation
primary productivity
Si_{xs}
Mn-oxides
and hydroxides
oxic
oxic
Mn-oxides and hydroxides
Mn in carbonate phases
SALINITY
TEMPERATURE
-
+
-
+
G
Above FISH LEVEL
Mn
Mn-oxides
and hydroxides
oxic
oxic
Mn-oxides and hydroxides
Mn in carbonate phases
SALINITY
TEMPERATURE
-
+
-
+
H
Above FISH LEVEL
oxic
oxic
SALINITY
TEMPERATURE
-
+
-
+

Figure 11b

Sections						
Name	Basin	Litholostratigraphic expression of the Jenkyns Event	avg TOC (%)	max TOC (%)	Palaeobathymetry	References
Sogno	Lombardy Basin (Italy)	5 m-thick organic-rich dark grey to black marl	0.8	2.4	about 1500 m	Erba et al., 2019b, 2022
Dogna	Belluno Basin (Italy)	no lithostratigraphy available	1.5	5.5	pelagic (not specified)	Jenkyns et al., 2001; Sabatino et al., 2009; Dickson et al., 2017
Peniche	Lusitanian Basin (Portugal)	marlstones and limestones with a 8 cm-thick black shale	2.6 *		carbonate ramp (hemipelagic)	Bjerrum et al., 2001; Hesselbo et al., 2007; Hermoso et al., 2009b
Creux de l'Ours	Sub-Briançonnais Basin (Switzerland)	dark grey laminated marly clay	2.5	5	hemipelagic	Fantasia et al., 2018, 2019b
Bächental	Bächental Basin (Austria)	black shales and bituminous marls	5	13	several hundred meters at the transition of distal slope to basin	Neumeister et al., 2015
Réka Valley	Mecsek Basin (Hungary)	parallel bedded calcareous black shales	5.5	14	hemipelagic (not specified)	Müller et al., 2017; Ruebsam et al., 2018
Sancerre	Paris Basin (France)	calcareous marlstones with several organic-rich intervals ("Schistes Carton Fm.")	7	11	restricted epicontinental sea	Hermoso et al., 2009a, 2012
Rietheim	Southern Tabular Jura (Switzerland)	organic-rich laminated marlstones; hiatus at the base of the Jenkyns Event ("Kartonschiefer-Fazies")	6	12	shallow water depths	Montero-Serrano et al., 2015; Fantasia et al., 2018
Dotternhousen	SW German Basin (Germany)	organic-rich marlstones and marly claystones ("Posidonienschiefer Fm." - Posidonia Shale)	10	15	50–150 m	Bandel and Knitter, 1986; Schouten et al., 2000; Röhl et al., 2001; Frimmel et al., 2004; Röhl and Schmid-Röhl, 2005; Dickson et al., 2017
Schandelah Core	SW German Basin (Germany)	dark grey, dark brown, black shales ("Posidonienschiefer Fm." - Posidonia Shale)	11	17.5	100 m	Bjerrum et al., 2001; Baroni et al., 2018; van Schootbrugge et al., 2019; Visentin et al., 2021
Yorkshire	Cleveland Basin (UK)	organic-rich laminated shales ("Jet Rock Fm.")	7.5	15	15 - 30 m	Hallam, 1967; Hesselbo et al., 2000; Cohen et al., 2004; Kemp et al., 2005; Dickson et al., 2017

* *TOC refers only to the sole 8 cm-thick black shale layer*

Table 1

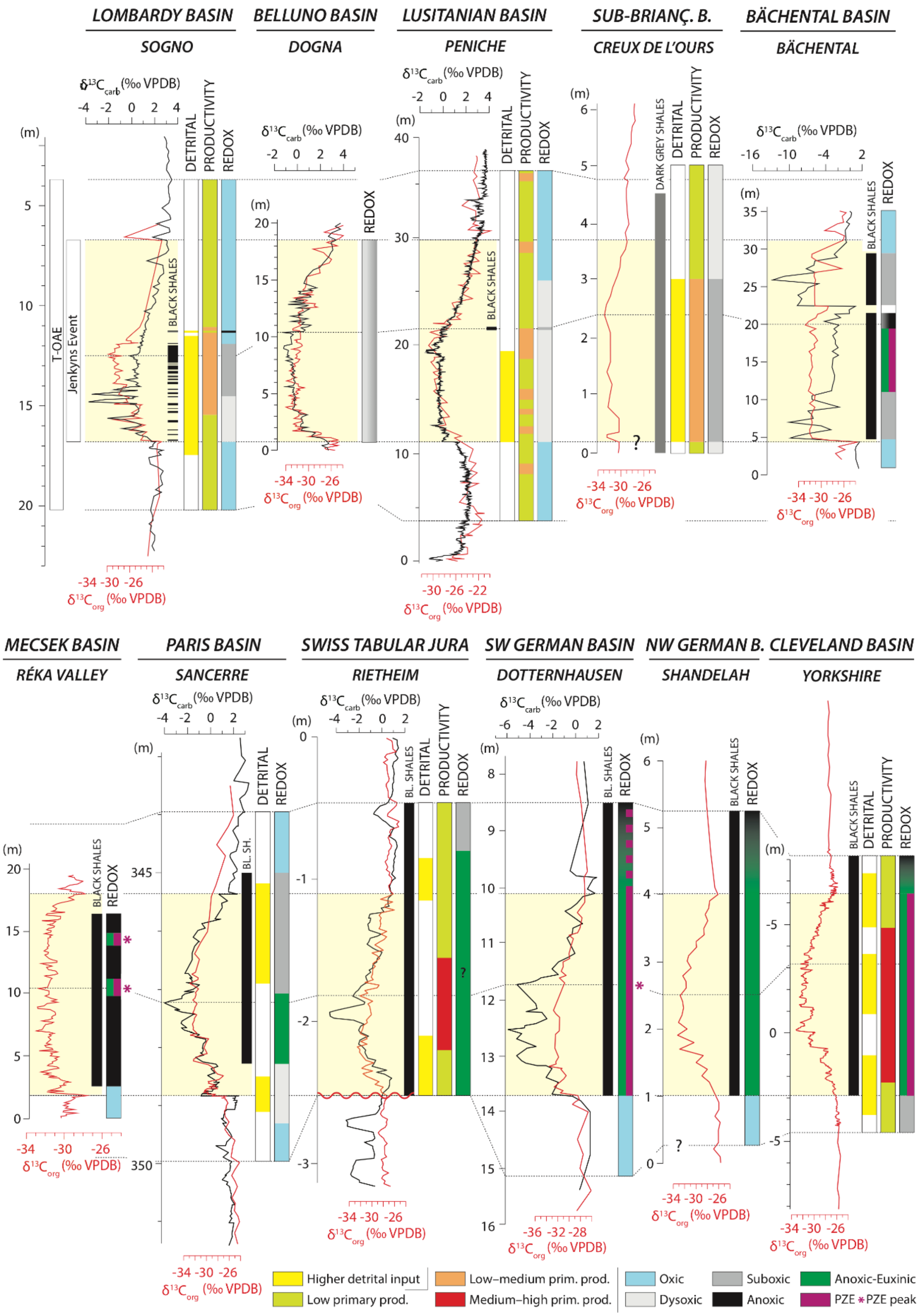

LOMBARDY BASIN
SOGNO
BELLUNO BASIN
DOGNA
LUSITANIAN BASIN
PENICHE
SUB-BRIANÇ. B.
CREUX DE L'OURS
BÄCHENTAL BASIN
BÄCHENTAL
MECSEK BASIN
RÉKA VALLEY
PARIS BASIN
SANCERRE
SWISS TABULAR JURA
RIETHEIM
SW GERMAN BASIN
DOTTERNHAUSEN
NW GERMAN B.
SHANDELAH
CLEVELAND BASIN
YORKSHIRE
$\delta^{13}C_{carb}$ (‰ VPDB)
$\delta^{13}C_{org}$ (‰ VPDB)
(m)
T-OAE
Jenkyns Event
BLACK SHALES
BL. SHALES
BL. SH.
DARK GREY SHALES
DETRITAL
PRODUCTIVITY
REDOX
?
Higher detrital input
Low primary prod.
Low–medium prim. prod.
Medium–high prim. prod.
Oxic
Dysoxic
Suboxic
Anoxic
Anoxic-Euxinic
PZE * PZE peak

Figure 12

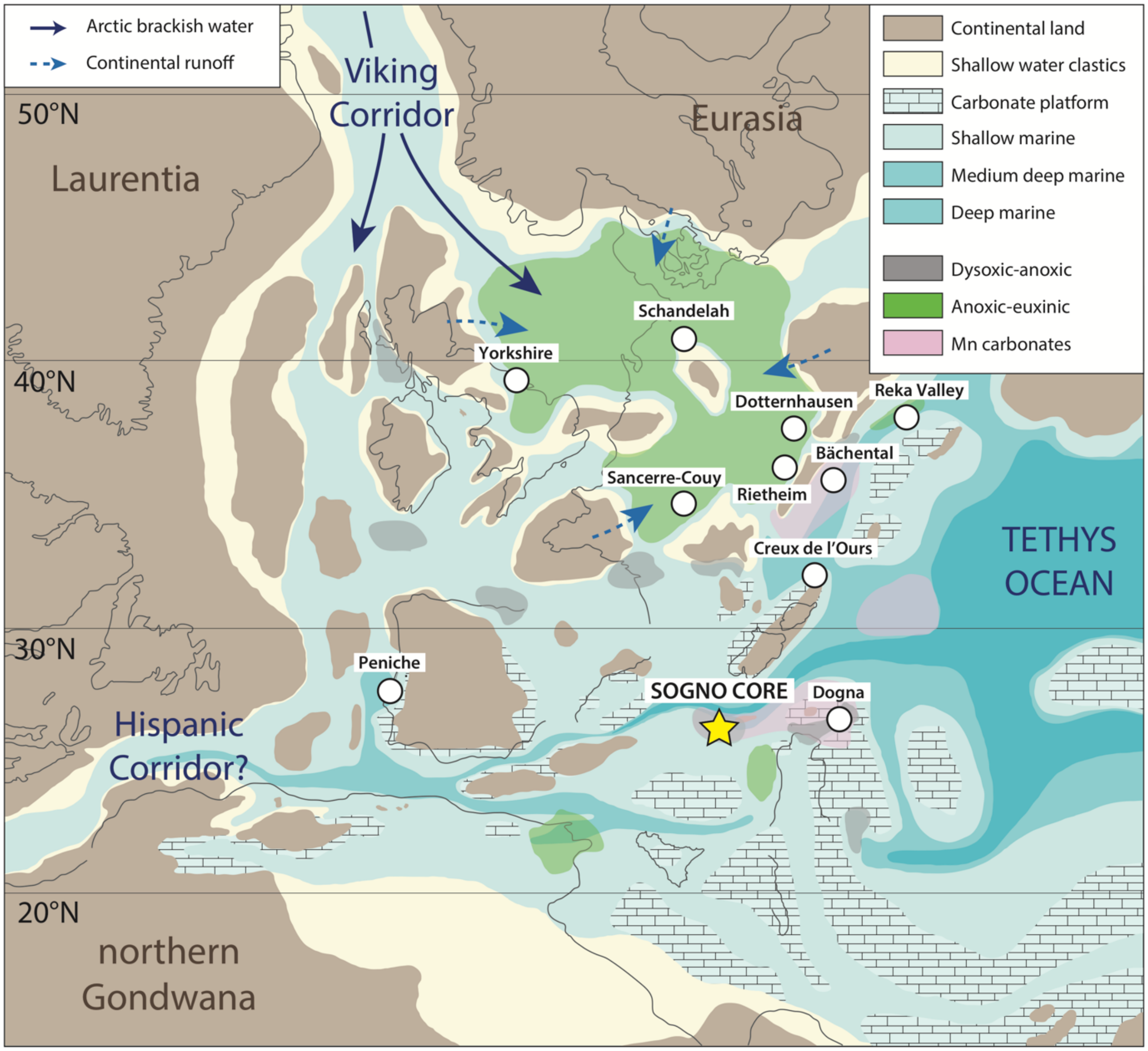

1690

1691 **Figure 13**